Supporting Information

The relationship between enzyme conformational change, proton transfer, and phosphoryl transfer in β-phosphoglucomutase.

Angus J. Robertson,[1, †, ‡] Alex L. Wilson,[2, ‡] Matthew J. Burn,[2] Matthew J. Cliff,[2] Paul L. A. Popelier,[2] and Jonathan P. Waltho*[1, 2]

[1] *Krebs Institute for Biomolecular Research, Department of Molecular Biology and Biotechnology, the University of Sheffield, Sheffield, S10 2TN, United Kingdom*

[2] *Manchester Institute of Biotechnology, Department of Chemistry, The University of Manchester, Manchester, M1 7DN, United Kingdom*

[†] *Current address: Laboratory of Chemical Physics, National Institute of Diabetes and Digestive and Kidney Diseases, National Institutes of Health, Bethesda, MD 20892, USA*

[‡] *These authors contributed equally towards this work*

* *Email*: j.waltho@sheffield.ac.uk

Contents

1. Protein production and purification

The *pgmB* gene from Lactococcus lactis together with the *pgmB* gene containing the D10N mutation were cloned in pET22b+ expression vectors and used to express βPGM_{WT} and βPGM_{D10N} proteins in *E. coli* strain BL21(DE3). One-liter cell cultures were grown to log phase in M9 media (with ^{15}N isotopic enrichment), induced with 1 mM IPTG and grown for a further 16 h at 25 °C. Perdeuterated protein preparations for enzyme dynamics were grown in 100% D_2O and included >97% ^2H isotope labelling of the carbon source, glucose (CortecNet). Cells were harvested by centrifugation at 10,000 rpm for 10 min at 4 °C, decanted and frozen at −80 °C. Cell pellets were resuspended in ice-cold standard native buffer (50 mM K^+ HEPES (pH 7.2), 5 mM $MgCl_2$, 2 mM NaN_3) supplemented with one tablet of complete TM protease inhibitor cocktail (Roche). The cell suspension was lysed on ice by sonication for 6 cycles of pulsation for 20 s with 60 s cooling intervals. The cell lysate was then separated by ultracentrifugation (Beckman Coulter Avanti centrifuge) at 24,000 rpm for 35 min at 4 °C to remove insoluble matter. The cleared cell lysate was filtered using a 0.2 μm syringe filter and loaded onto a DEAE-Sepharose fast flow ion exchange column connected to an ÄKTA purification system that had been washed previously with 1 column volume of 6 M guanidine hydrochloride (GuHCl), 1 column volume of 1 M NaOH and equilibrated with > 2 column volumes of standard native buffer. Following extensive washing, proteins bound to the DEAE-Sepharose column were eluted with a gradient of 0 to 100% standard native buffer containing 0.5 M NaCl. Fractions containing βPGM were checked for purity using SDS-PAGE, were pooled together and concentrated by Vivaspin (10 kDa MWCO). The protein sample was filtered using a 0.2 μm syringe filter and loaded onto a prepacked Hiload 26/60 Superdex 75 size-exclusion column connected to an ÄKTA purification system that had been pre-equilibrated with filtered and degassed standard native buffer containing 1 M NaCl. βPGM eluted as a single peak and fractions containing βPGM were checked for purity using SDS-PAGE, were pooled together, buffer exchanged into standard native buffer and concentrated to 1 mM by Vivaspin (10 kDa MWCO) for storage as 1 mL aliquots at −20 °C. The overall yield for βPGM was ca. 60 mg protein from 1 L of bacterial culture.

2. Obtaining QM$_{WT}$ PO$_3$ and QM$_{D10N}$ PO$_3$ models of the active site

A quantum mechanical (QM) model was constructed starting from the X-ray crystal structure of β-phosphoglucomutase inhibited with glucose-6-phosphate (G6P) and aluminium tetrafluoride (AlF$_4^-$) (2WF6: 1.4 Å). This contains a transition state analogue (TSA) of βG16BP, whereby AlF$_4^-$ is used in place of the transferring phosphate (PO$_3^-$) group to trap the transition state conformation. Amino acid residues not contributing to the stabilisation of the active site through key hydrogen bonding interactions were removed, and AlF$_4^-$ was replaced with PO$_3^-$. Specifically, G6P, a catalytic Mg^{2+} ion, 10 amino acid residues (D8, L9, D10, G46, V47, S114, A115, K145, E169, and D170), and 2 explicit water molecules (2210, 2211) were included (Figure 2 in the main paper and Figure S1). To guide the fixed boundary positions of our QM$_{WT}$ PO$_3$ model, NMR-derived order parameters (S^2 values) were determined for the βPGM$_{WT}$:AlF$_4$:G6P complex in solution, under conditions reported for its backbone resonance assignment (Table S1, BMRB:15467 [1]). These order parameters measure the degree of local rigidity of backbone amide groups on a sub-nanosecond timescale. In the QM$_{WT}$ PO$_3$ model, fixed atoms were always ≤ 2 atoms from a well ordered (S^2 > 0.8) amide. The resulting active site QM model contained 163 atoms. All fixed atoms are denoted with an asterisk (*) in Figure S1. The TS search was performed with GAUSSIAN09 using the B3LYP hybrid functional formulation of Kohn-Sham Density Functional Theory (KS-DFT).[2-6] A cc-pVDZ basis set was used for all atoms, excepting atoms for which more care was given due to reaction importance. Specifically, oxygen atoms expected to have more negative charge density were described by aug-cc-pVDZ (E169, D170, distal PO$_3^-$), and those in residues directly involved in bond-making/bond-breaking were described by aug-cc-pVTZ (D8, D10, transferring PO$_3^-$, O1$_{G6P}$). The structure was considered optimised when the force on all nuclei fell below 1 μHartree/Bohr. The SCF was considered converged when the density matrix residual was less than 10^{-7}. This procedure gave a converged TS model with a harmonic vibrational value of 158i cm^{-1} corresponding to motion along the reaction coordinate. In freezing certain Cartesian coordinates, there were a small number of non-relevant imaginary frequencies (67i, 32i, 27i, 15i, 8i cm^{-1}). Snapshots of the vibrational mode corresponding to motion along the reaction coordinate were taken at regular O1$_{G6P}$-P1$_{PO3}$-OD1$_{D8}$ intervals (0.14 Å), with single point energies evaluated for each of the 9 resulting structures, using the same level of theory and basis set as in the TS search. Coordinates for the 9 resulting structures have been uploaded as PDB files and an animation of the reaction trajectory is provided as a GIF (**File names:** QMWT_PO3_model_str_1.pdb to QMWT_PO3_model_str_9.pdb, and QMWT_PO3_model_TS_vibr.gif). QM$_{WT}$ PO$_3$ model overlaid with 2WF6 is shown (Figure S2, non-H atom RMSD: 0.16 Å).

An additional QM model was constructed in exactly the same way as the QM$_{WT}$ PO$_3$ model (with the same atoms included and level of theory used), but in the NAC III conformation (PDB: 5O6P). As the crystal structure contains the N10 mutation, this was swapped for a protonated D10, in line with WT. The structure was then optimised to a ground state, under the same conditions as above.
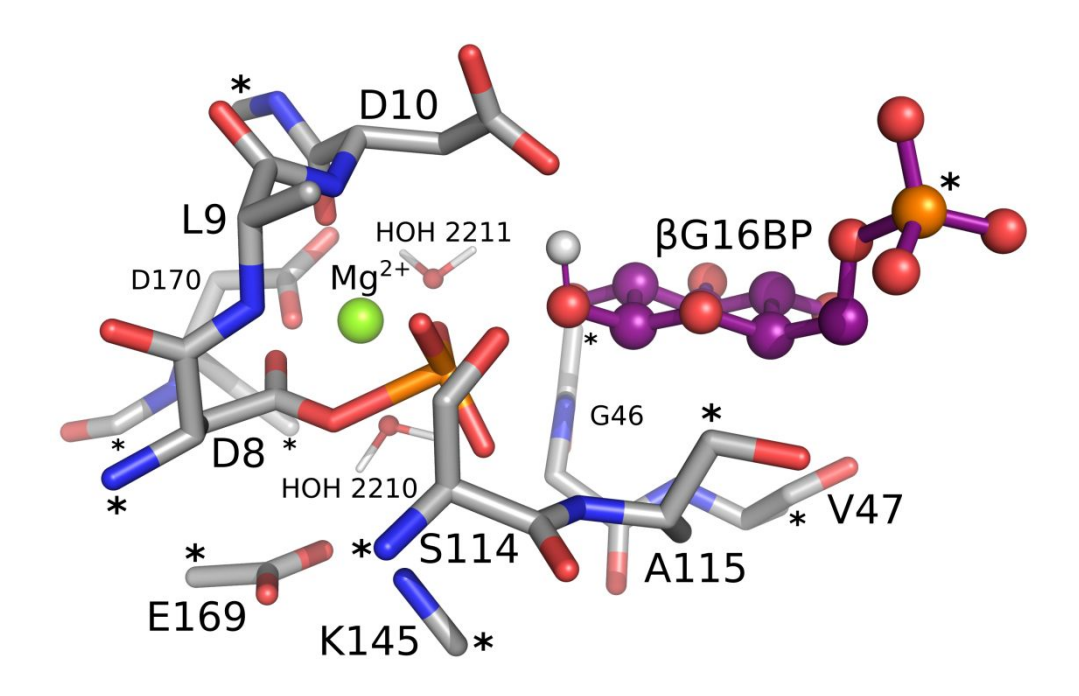
Figure S1. The 163 atom active site model for the phosphoryl transfer reaction between βG16BP and residue D8. Selected active site residues (and waters) are shown as sticks in standard CPK colours, with carbons (grey), phosphorus (orange), oxygen (red), nitrogen (blue), and magnesium (light green). The G6P ligand is shown with purple carbon atoms (for clarity). All fixed atoms are denoted with an asterisk (*).

Table S1. TSA derived backbone order parameter (S^2) values for the active site residues included in the QM_{WT} PO_3 model. While not perfect, the S^2 values determined in the βPGM_{WT}:AlF$_4$:G6P and βPGM_{WT}:AlF$_4$:G6P TSA complexes indicate that the active site is held relatively rigidly (on the ps-ns timescale) when the protein adopts transition state architecture. This suggests that minimal errors are introduced by truncating and fixating the residues as shown in Figure S1.

Residue	WT	D10N
8	0.826±0.003	0.831±0.002
9	0.857±0.004	-
10	0.842±0.008	-
46	0.851±0.002	0.824±0.004
47	0.801±0.001	0.811±0.002
114	0.817±0.001	0.806±0.002
115	-	-
145	0.839±0.003	-
169	0.809±0.002	0.808±0.003
170	0.810±0.002	0.780±0.002
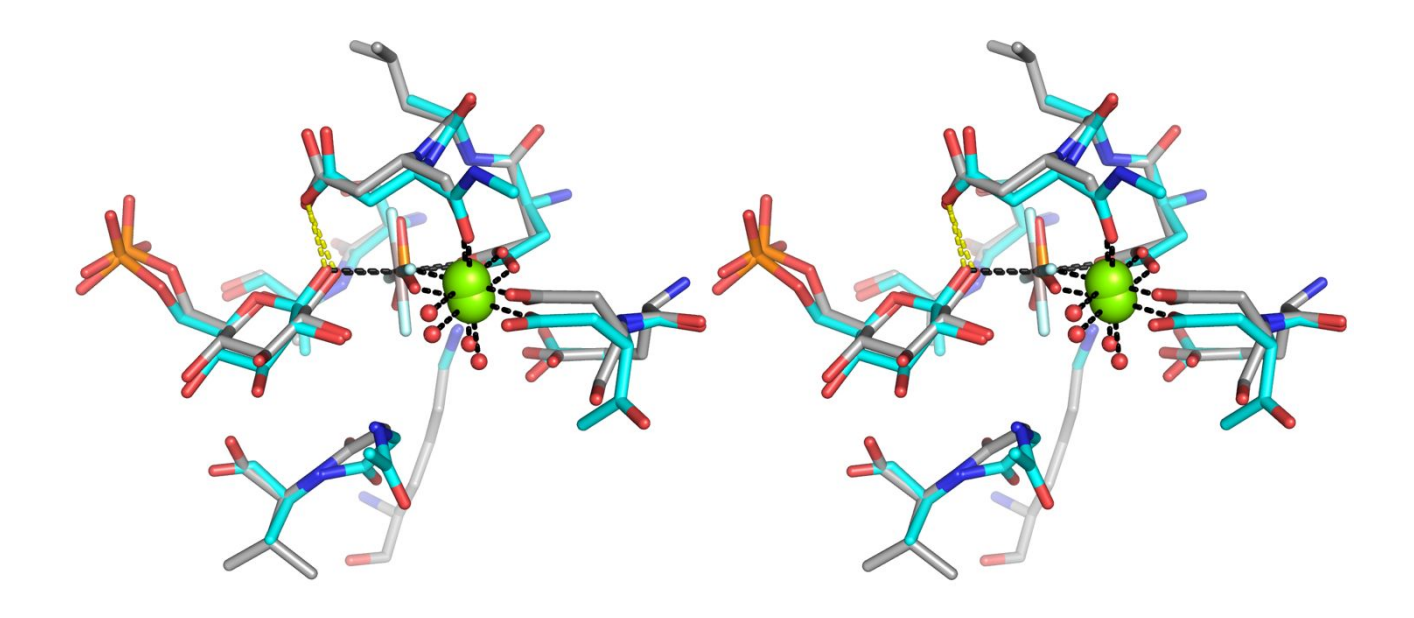
Figure S2. Crosseye stereo representation of QM_{WT} PO_3 model (cyan carbon atoms) overlaid with βPGM_{WT}:AlF_4:G6P structure (PDB: 2WF6; grey carbon atoms). Standard CPK colouring of non-carbon atoms is used with metal coordination indicated by black dashed lines and selected hydrogen bonds illustrated as yellow dashed lines.

A second QM model was made by substituting D10 for N10 (164 atoms). This substitution of the GAB has been shown experimentally to resist proton transfer.[7] X-Ray crystallographic investigations of a TSA containing this mutation (βPGM_{D10N}:AlF_4:G6P, PDB:5OK2, 1.1 Å) suggest that the N10 carboxamide group is orientated so as to form a HT1-$O1_{G6P}$ hydrogen bond to a deprotonated $O1_{G6P}$ atom (Figure S5). This orientation and protonation state is therefore maintained in the QM_{D10N} PO_3 model. An exhaustive TS search was conducted in order to establish the trajectory for the mutant, without success. During all attempts, prevention of protonation of $O1_{G6P}$ leaving group caused collapse back to a GS_{12}-like geometry. Instead, the wild-type reaction trajectory established above was modified (D10 > N10) at each step, before re-optimisation and re-evaluation of single point energies, utilising the same level of theory and basis sets described above. The final model is shown, overlaid with PDB: 6L03 X-ray crystal structure (Figure S3, non-H atom RMSD: 0.15 Å).

Figure S3. Crosseye stereo representation of QM_{D10N} PO_3 model (deprotonated $O1_{G6P}$; cyan carbon atoms) overlaid with βPGM_{D10N}:AlF_4:G6P structure (PDB: 6L03; grey carbon atoms). Standard CPK colouring of non-carbon atoms is used with metal coordination indicated by black dashed lines and selected hydrogen bonds illustrated as yellow dashed lines.
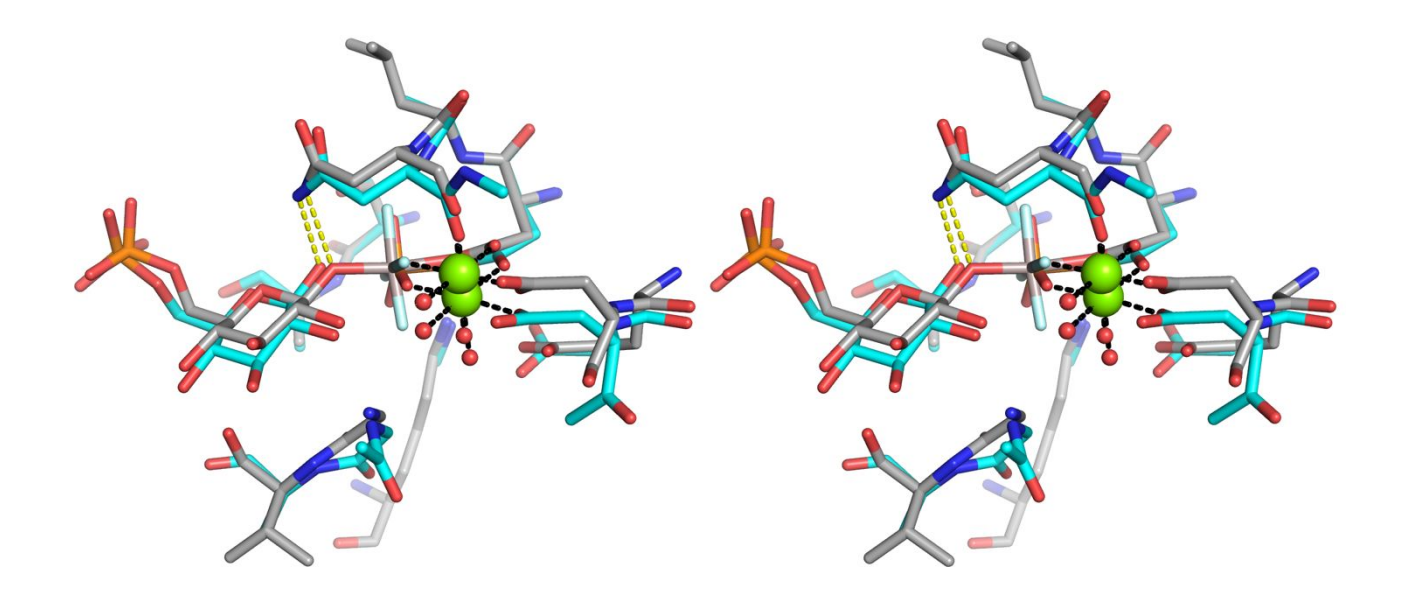
3. Interacting Quantum Atoms (IQA) and Quantum Chemical Topology (QCT)

Quantum Chemical Topology (QCT)[8,9] is a methodology that extracts chemical insight from modern wavefunctions using ideas from the mathematical branch of dynamical systems. QCT defines atoms inside a system (molecule, molecular assembly or any condensed matter). The gradient of the electron density traces paths of steepest ascent in the electron density, the majority of which terminate at a nucleus. The subspace occupied by such a bundle gradient paths constitutes a so-called topological atom, or just atom. In this manner, every portion of space is assigned to an atom and there is no spatial overlap between atoms. In other words, this partitioning is space-filling and thus each bit of electron density is assigned to an atom. The energies of all atoms thus add up to reproduce the total energy of the original wavefunction. Atomic net charges are also clearly defined as the electron density within an atom's volume, while corrected for nuclear charge.

Atomic charges were calculated using the AIMAll17 program (Tables S2-S4)[10] using either the PROAIM or PROMEGA integration method implemented in AIMAll17, while the integral of the Laplacian of the electron density in each atom was kept below 1×10^{-3} Hartrees. The energy partitioning method we used is called Interacting Quantum Atoms (IQA)[11]. IQA is a part of QCT and also been implemented in AIMAll17, which returns both intra- and interatomic energy contributions, providing a rigorous quantification of both electrostatic and covalent contributions to atomic interactions (Equations S3.1 - S3.6)[11]. Equation S3.1 shows how a system's total energy (E_{WFN}) is fully described by only intra- (E_{intra}) and inter-atomic (V_{inter}) energy contributions,

$$E_{WFN} \; ; \; E_{IQA} = \sum_{A}^{n} E_{\text{intra}}^{A} + \frac{1}{2} \sum_{A}^{n} \sum_{B \neq A}^{n} V_{\text{inter}}^{AB} \qquad [\text{S3.1}]$$

where n is the number of atoms of the total system. The intra-atomic energy contribution is further decomposed as follows

$$E_{\text{intra}}^{A} = T^{A} + V_{ne}^{AA} + V_{ee}^{AA} \qquad [\text{S3.2}]$$

where T^{A} is the atomic kinetic energy, V_{ne}^{AA} represents (intra-atomic) electron-nuclear interactions while V_{ee}^{AA} represents (intra-atomic) electron-electron interactions. Similarly, the inter-atomic energy is decomposed as follows,

$$V_{\text{inter}}^{AB} = V_{nn}^{AB} + V_{ne}^{AB} + V_{en}^{AB} + V_{ee}^{AB} \qquad [\text{S3.3}]$$

where V_{nn}^{AB} accounts for nuclear-nuclear interactions, while V_{ne}^{AB} accounts for the interaction between the nucleus of atom A and the electrons of atom B, and V_{en}^{AB} accounts for interaction between the nucleus of atom B and the electrons of atom A. Finally, V_{ee}^{AB} accounts for electron-electron interactions and can be written as the sum of Coulomb (V_{Coul}^{AB}) and exchange-correlation (V_{xc}^{AB}) interactions or

$$V_{ee}^{AB} = V_{Coul}^{AB} + V_{xc}^{AB} \qquad \text{[S3.4]}$$

We have now separated out the exchange-correlation interaction from the four classical electrostatic interactions (summarised as V_{cl}^{AB}),

$$V_{cl}^{AB} = V_{nn}^{AB} + V_{ne}^{AB} + V_{en}^{AB} + V_{Coul}^{AB} \qquad \text{[S3.5]}$$

giving the total interaction energy term,

$$V_{inter}^{AB} = V_{cl}^{AB} + V_{xc}^{AB} \qquad \text{[S3.6]}$$

where V_{cl}^{AB} represents the ("classical") electrostatic interaction between atoms A and B, and V_{xc}^{AB} represents exchange-correlation energy, a measure of covalency, between atoms A and B.

Finally, V_{xc}^{AB} can be related to bond order (δ)[12],

$$\delta^{AB} \; ; \; -2RV_{xc}^{AB} \qquad \text{[S3.7]}$$

A comprehensive list of all atomic net charges, IQA energy contributions, and bond orders are available upon request.

Table S2. QTAIM net atomic partial charges (in e or a.u.) for the QM_{WT} PO_3 model.

	Net Charge		
Atom	**GS_{12}**	**TS_{23}**	**GS_{34}**
$P1_{PO3}$	3.72	3.69	3.71
$O1_{G6P}$	-1.23	-1.16	-1.17
$OD1_{D8}$	-1.25	-1.22	-1.23
$OD2_{D8}$	-1.29	-1.28	-1.27
$OD2_{D10}$	-1.22	-1.23	-1.24
$O1_{PO3}$	-1.57	-1.58	-1.58
$O2_{PO3}$	-1.51	-1.51	-1.51
$O3_{PO3}$	-1.53	-1.52	-1.52
HT1	0.67	0.66	0.66
CD_{D8}	1.75	1.69	1.68
$C1_{G6P}$	0.95	1.03	1.05

Table S3. QTAIM net atomic partial charges (in e or a.u.) for the QM_{D10N} PO_3 model.

	Net Charge		
Atom	**GS_{12}'**	**TS_{23}'**	**GS_{34}'**
$P1_{PO3}$	3.71	3.67	3.70
$O1_{G6P}$	-1.20	-1.12	-1.13
$OD1_{D8}$	-1.25	-1.22	-1.23
$OD2_{D8}$	-1.30	-1.28	-1.28
$ND2_{N10}$	-1.29	-1.28	-1.28
$O1_{PO3}$	-1.58	-1.59	-1.59
$O2_{PO3}$	-1.52	-1.52	-1.52
$O3_{PO3}$	-1.54	-1.53	-1.52
HT1	0.57	0.57	0.57
CD_{D8}	1.76	1.71	1.69
$C1_{G6P}$	0.97	1.05	1.07

Table S4. QTAIM net atomic partial charges (in e or a.u.) for the (A) QM_{WT} AlF_4 model, (B) QM_{D10N} AlF_4 model and (C) QM_{D10N} AlF_4 protonated model.

	Net Charge		
Atom	**A**	**B**	**C**
Al_{AlF4}	2.65	2.64	2.65
$O1_{G6P}$	-1.14	-1.24	-1.06
$OD1_{D8}$	-1.20	-1.18	-1.23
$OD2_{D10}$	-1.08	-1.10	-1.09
$F1_{AlF4}$	-0.93	-0.93	-0.92
$F2_{AlF4}$	-0.88	-0.88	-0.89
$F3_{AlF4}$	-0.89	-0.89	-0.89
$F4_{AlF4}$	-0.89	-0.89	-0.89
HT1	0.62	0.51	0.44

4. REG Analysis of IQA Energy Terms

Overall, the IQA energy decomposition returns a total of n^2 intra- and inter-atomic energy terms that add up to return the total IQA energy of an n atom system. Therefore, the 163 atom QM_{WT} PO_3 model has 26,569 intra- and inter-atomic terms for each of the 9 snapshots across the reaction coordinate (26,896 for the 164 atom QM_{D10N} PO_3 model). The Relative Energy Gradient (REG)[13] method, implemented in the program ANANKE, was developed in the Popelier group to systematically, and without bias, rank energy terms according to their importance in shaping the behaviour of a chemical process. For example, one can ask how and why two DNA base pairs are held together: are hydrogen bonds sufficient? If so, then the energy profile of only those atoms involved in the hydrogen bonds should drive the profile of the total system. This question can be answered by comparing, over a given dynamical change in the system, the energy gradient of the subsystem (i.e. the hydrogen bond) and that of the total system. For example, the DNA base pairs can be pulled apart (i.e. dynamical change) and the two gradients (subsystem and total system) can be compared by calculating their ratio. These ratios can then be ranked from high to low. The highest ranked ratios correspond to the energy contributions that most drive the total system. Hence, they best explain the behaviour of the total system. They thus offer chemical insight by revealing which energy type (electrostatic, covalent, …) and its locale, is governing the total system.

Equation S4.1 describes the total energy of a given molecular system as the summation of each energy contribution, where s is a pre-defined coordinate (e.g. a dihedral angle or inter-nuclear separation) controlling the dynamical change,

$$E(s) = \sum_i E_i(s) \qquad \text{[S4.1]}$$

Practically speaking, each integration carried out in the IQA framework and delivering an energy contribution E_i, has an associated computational error such that $E(s) \neq \sum_i E_i(s)$. These errors are additive and total errors are usually small (~1 kJ/mol for a water dimer[13]) such that the original total energy is well recovered.

Each IQA energy term $E_i(s)$ is related to the total wavefunction energy $E(s)$ via linear regression,

$$E_i(s) = m_{REG_i} E(s) + c_i \qquad \text{[S4.2]}$$

and the gradient (m_{REG_i}) is given the shorthand the "REG value". This value is obtained by an ordinary least-squares linear regression, to the M data points representing the chemical process of interest, or

$$m_{REG_i} = \frac{(\mathbf{E}^{translated})^\tau \cdot \mathbf{E}_i^{translated}}{(\mathbf{E}^{translated})^\tau \cdot \mathbf{E}^{translated}} \qquad \text{[S4.3]}$$

where

$$\mathbf{E}^{translated,\tau} = \begin{bmatrix} E(s_1) - \overline{E}(s) & E(s_2) - \overline{E}(s) & ... & E(s_M) - \overline{E}(s) \end{bmatrix} \qquad \text{[S4.4]}$$

$$\mathbf{E}_i^{translated,\tau} = \begin{bmatrix} E_i(s_1) - \overline{E}_i(s) & E_i(s_2) - \overline{E}_i(s) & ... & E_i(s_M) - \overline{E}_i(s) \end{bmatrix} \qquad \text{[S4.5]}$$

and the superscript bar represents the average over the M data points. The Pearson coefficient (R_i) is then used to determine the degree of correlation between an energy contribution and the total energy:

$$R_i = \frac{\sum_s^M \left[E(s) - \overline{E}(s) \right] \left[E_i(s) - \overline{E}_i(s) \right]}{\sqrt{\sum_s^M \left[E(s) - \overline{E}(s) \right]^2} \sqrt{\sum_s^M \left[E_i(s) - \overline{E}_i(s) \right]^2}} \qquad \text{[S4.6]}$$

Note that REG values are only chemically interpretable when this correlation is significant. In the present work, all correlations are > 0.95.

REG values can be positive or negative. Positive values occur when the gradient of a particular energy contribution has the same sign as the total energy, negative values *vice versa*. For segment 2 in the QM_{WT} PO_3 model, in terms of the overall energy profile, TS_{23} is destabilised relative to GS_{12} and so, generally, energy terms that are also significantly destabilised between these two stationary points have a large positive REG value. In segment 3, GS_{34} is stabilised relative to TS_{23}, so energy terms with large positive REGs must be stabilised in GS_{34} relative to TS_{23}, although the energy difference between GS_{34} and TS_{23} is only ~ 1 kJ/mol. For segment 2 in the QM_{D10N} PO_3 model, TS_{23}' is destabilised relative to GS_{12}', so energy terms that are also destabilised between these two stationary points have a positive REG. In segment 3, GS_{34}' is destabilised relative to TS_{23}', so energy terms with positive REGs must also be destabilised.

In Tables S5 and S6, the energy terms with the largest positive and negative REG values are listed for both the QM_{WT} PO_3 and QM_{D10N} PO_3 models. REG values are used to identify the energy terms that contribute most to the shape of the overall energy profile, either constructively (positive REG value) or destructively (negative REG value). Once these terms have been isolated, we can compare the relative energy changes between stationary points. Each term is coloured according to its change in energy.

Table S5. Energy terms with the largest positive and negative REG values between defined points on the energy profile of the QM_{WT} PO_3 model, colour coded to match Figure 4 in the main paper. ΔE represents the difference in a given energy term between TS_{23} and GS_{12}, or GS_{34} and TS_{23}. Red indicates that the energy term increases (becomes more positive, or less negative) from $GS_{12} \rightarrow TS_{23}$ or $TS_{23} \rightarrow GS_{34}$. Blue indicates that the energy term decreases (becomes less positive, or more negative) from $GS_{12} \rightarrow TS_{23}$ or $TS_{23} \rightarrow GS_{34}$.

$GS_{12} \rightarrow TS_{23}$			$TS_{23} \rightarrow GS_{34}$		
Energy term	REG	ΔE (kJ/mol)	Energy term	REG	ΔE (kJ/mol)
V_{cl} (O1$_{G6P}$-P1$_{PO3}$)	34.3	1252.5	V_{cl} (P1$_{PO3}$-OD1$_{D8}$)	479.6	-323.1
V_{cl} (OD1$_{D8}$-CD$_{D8}$)	9.4	343.2	V_{cl} (P1$_{PO3}$-OD2$_{D8}$)	85.6	-57.6
V_{cl} (P1$_{PO3}$-CD$_{D8}$)	7.9	295.7	V_{cl} (C1$_{G6P}$-O1$_{G6P}$)	79.9	-53.8
V_{cl}(OD2$_{D10}$-P1$_{PO3}$)	5.0	184.5	V_{xc} (P1$_{PO3}$-OD1$_{D8}$)	63.2	-42.5
V_{xc} (O1$_{G6P}$-P1$_{PO3}$)	4.6	167.3	V_{cl} (HT1-P1$_{PO3}$)	62.7	-42.2
V_{cl} (O1$_{G6P}$-O2$_{PO3}$)	-5.4	-196.3	V_{cl} (O3$_{PO3}$-OD1$_{D8}$)	-77.7	52.3
V_{cl} (O1$_{G6P}$-O1$_{PO3}$)	-5.4	-198.5	V_{cl} (O2$_{PO3}$-OD1$_{D8}$)	-77.8	52.4
V_{cl} (O1$_{G6P}$-O3$_{PO3}$)	-5.7	-206.1	V_{cl} (O1$_{PO3}$-OD1$_{D8}$)	-80.4	54.1
V_{cl} (HT1-P1$_{PO3}$)	-6.8	-248.2	E_{intra} (P1$_{PO3}$)	-144.9	97.6
E_{intra} (O1$_{G6P}$)	-7.8	-282.6	V_{cl} (O1$_{G6P}$-P1$_{PO3}$)	-149.0	100.4
V_{cl} (P1$_{PO3}$-OD1$_{D8}$)	-13.3	-509.4	V_{cl} (P1$_{PO3}$-CD$_{D8}$)	-176.6	118.9

Table S6. Energy terms with the largest positive and negative REG values between defined points on the energy profile of the QM_{D10N} PO_3 model, colour coded to match Figure 4. ΔE represents the difference in a given energy term between TS_{23}' and GS_{12}', or GS_{34}' and TS_{23}'. Red indicates that the energy term increases (becomes more positive, or less negative) from GS_{12}' $\rightarrow$ TS_{23}' or TS_{23}' $\rightarrow$ GS_{34}'. Blue indicates that the energy term decreases (becomes less positive, or more negative) from GS_{12}' $\rightarrow$ TS_{23}' or TS_{23}' $\rightarrow$ GS_{34}'.

GS_{12}' $\rightarrow$ TS_{23}'			TS_{23}' $\rightarrow$ GS_{34}'		
Energy term	REG	ΔE (kJ/mol)	Energy term	REG	ΔE (kJ/mol)
V_{cl} (O1$_{G6P}$-P1$_{PO3}$)	11.8	1265.6	V_{cl} (P1$_{PO3}$-CD$_{D8}$)	7.7	118.5
V_{cl} (OD1$_{D8}$-CD$_{D8}$)	3.4	351.0	E_{intra} (P1$_{PO3}$)	7.0	107.7
V_{cl} (P1$_{PO3}$-CD$_{D8}$)	2.8	297.6	V_{cl} (O1$_{G6P}$-P1$_{PO3}$)	4.8	74.8
V_{cl} (P1$_{PO3}$-ND2$_{N10}$)	2.4	252.9	V_{cl} (OD1$_{D8}$-CD$_{D8}$)	3.6	55.5
V_{xc} (O1$_{G6P}$-P1$_{PO3}$)	1.7	172.0	V_{cl} (O1$_{PO3}$-OD1$_{D8}$)	3.3	51.5
V_{cl} (O1$_{G6P}$-O2$_{PO3}$)	-1.8	-195.5	V_{cl} (O2$_{PO3}$-OD1$_{D8}$)	2.6	39.6
V_{cl} (O1$_{G6P}$-O1$_{PO3}$)	-1.9	-199.5	V_{cl} (O3$_{PO3}$-OD1$_{D8}$)	2.5	39.3
V_{cl} (O1$_{G6P}$-O3$_{PO3}$)	-2.0	-210.9	V_{xc} (P1$_{PO3}$-OD1$_{D8}$)	-2.8	-44.0
E_{intra} (O1$_{G6P}$)	-3.2	-348.9	V_{cl} (C1$_{G6P}$-O1$_{G6P}$)	-2.9	-45.3
V_{cl} (P1$_{PO3}$-OD1$_{D8}$)	-4.7	-503.0	V_{cl} (P1$_{PO3}$-OD2$_{D8}$)	-3.8	-59.0
			V_{cl} (P1$_{PO3}$-OD1$_{D8}$)	-20.3	-313.9

5. Obtaining QM$_{WT}$ AlF$_4$, QM$_{D10N}$ AlF$_4$, and QM$_{D10N}$ AlF$_4$ protonated models of the active site

In the QM$_{WT}$ PO$_3$ model, PO$_3^-$ was resubstituted for AlF$_4^-$ to generate a QM$_{WT}$ AlF$_4$ model. As the model was reoptimised to a ground state, rather than a transition state, computational demand was decreased, allowing for 10 additional distal amino acid residues (G11, V12, T16, A17, H20, K45, S48, A113, S116, and S171) and 4 explicit water molecules to be included so that the final model contained 386 atoms (Figure S4, non-H atom RMSD: 0.05 Å). NMR derived order parameters (S^2 values), determined for the βPGM$_{WT}$:AlF$_4$:G6P complex in solution, were again used to guide fixed boundary positions. In the QM$_{WT}$ AlF$_4$ model, fixed atoms were always ≤ 2 atoms from a well ordered (S$^2 > 0.8$) amide (Table S7). All truncated amino acid residues were capped with methyl groups, with the carbon atom held fixed during geometry optimisation to mimic the structural rigidity provided by the deleted amino acid residues. This resulted in a total of 14 fixed carbon atoms. The G6P phosphorous atom was also held fixed, in its crystallographically determined coordinates. Geometry optimisation was performed with GAUSSIAN09 using the B3LYP hybrid functional formulation of Kohn-Sham Density Functional Theory (KS-DFT).[2-6] A 6-31G basis set was used for all atoms except fluorine, which was treated with a 6-31+G(d) basis set. Diffuse functions were added for fluorine to improve the agreement of calculated ^{19}F NMR chemical shifts with experiment. The structure was considered optimised when the forces on all nuclei fell below 1 μHartree/Bohr. The SCF was considered converged when the density matrix residual was less than 10^{-7}. To create a model for the D10N complex, D10 was replaced with N10. The resulting 387 atom QM$_{D10N}$ AlF$_4$ model was then reoptimised as above (Figure S5, non-H atom RMSD: 0.04 Å). In an additional model, D10 was replaced by N10 and O1$_{G6P}$ was protonated, before the protonated 388 atom QM$_{D10N}$ AlF$_4$ model was reoptimised, as above (Figure S6, non-H atom RMSD: 0.04 Å). Coordinates for the QM$_{WT}$ AlF$_4$ and QM$_{D10N}$ AlF$_4$ models are available on request (j.waltho@sheffield.ac.uk).

Table S7. Points of truncation in the active site model compared to NMR derived backbone order parameters. No residues showed significant mobility proximal to the points of truncation.

Fixed point	Closest S^2 parameter	WT S^2	D10N S^2
At CO of F7	NH of D8	0.83	0.83
At CA of I13	NH of I13	0.80	0.78
At CO of D15	NH of T16	0.80	0.75
At CA of E18	NH of E18	0.85	0.80
At CO of Y19	NH of H20	0.90	0.81
At CA of F21	NH of F21	0.84	0.81
At CO of L44	NH of K45	0.81	0.80
At CA of R49	NH of R49	0.85	0.85
At CO of L112	NH of A113	0.84	0.81
At CA of K117	NH of K117	-	0.79
At CO of S144	NH of K145	0.84	-
At CA of P146	NA	-	-
At CO of L168	NH of E169	0.81	0.81
At CA of Q172	NH of Q172	0.84	0.82
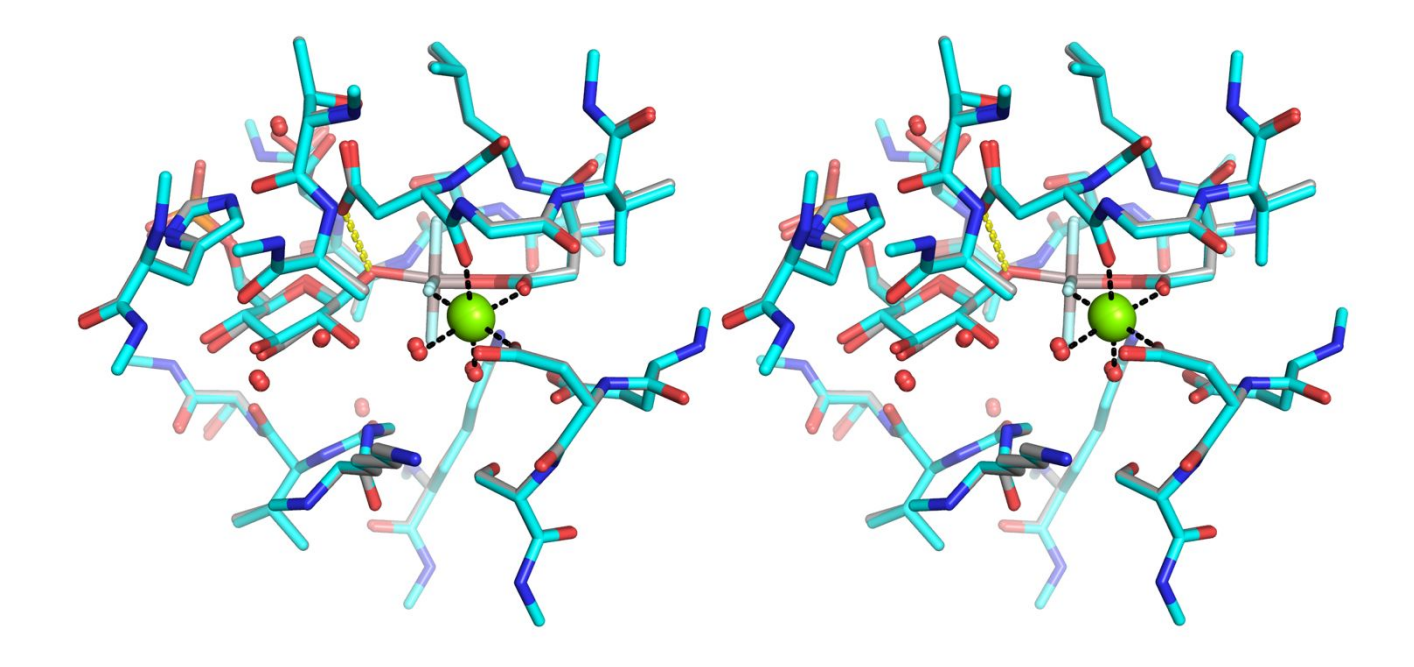
Figure S4. Crosseye stereo representation of QM_{WT} AlF_4 model (cyan carbon atoms) overlaid with βPGM_{WT}:AlF_4:G6P structure (PDB: 2WF6; grey carbon atoms). Standard CPK colouring of non-carbon atoms is used with metal coordination indicated by black dashed lines and selected hydrogen bonds illustrated as yellow dashed lines.
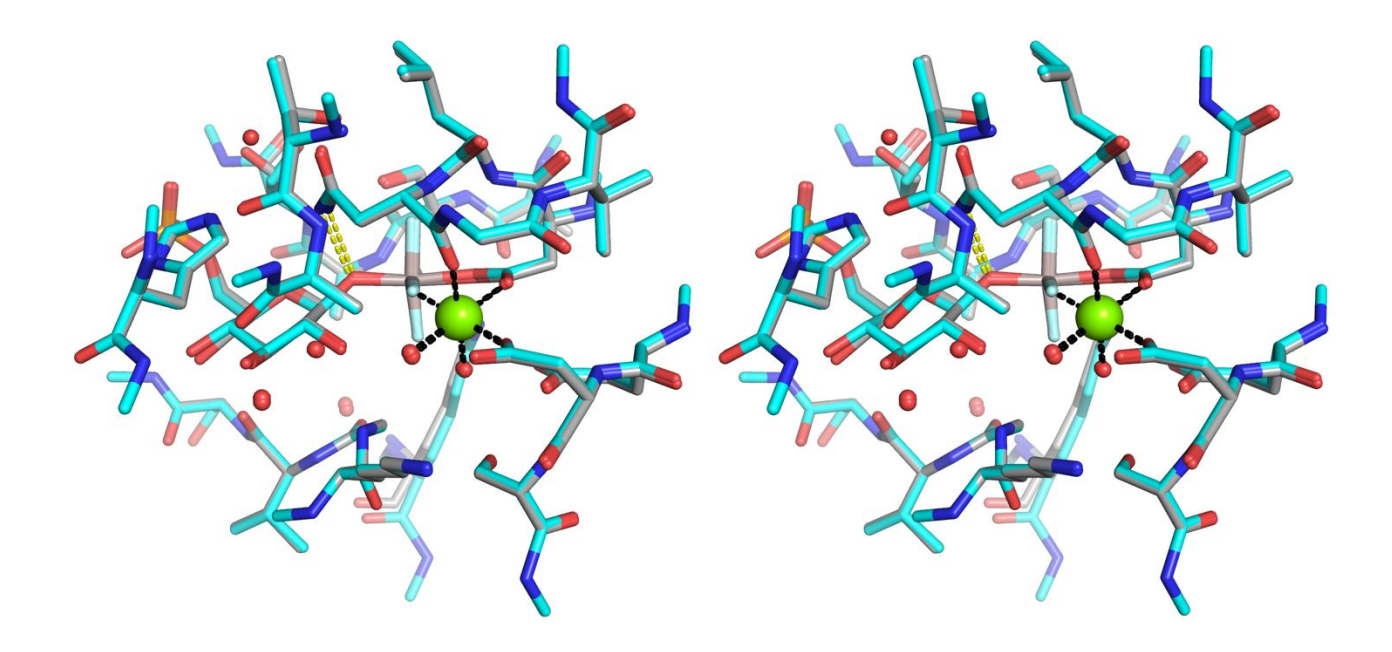
Figure S5. Crosseye stereo representation of QM_{D10N} AlF_4 model (deprotonated $O1_{G6P}$; cyan carbon atoms) overlaid with βPGM_{D10N}:AlF_4:G6P structure (PDB: 6L03; grey carbon atoms). Standard CPK colouring of non-carbon atoms is used with metal coordination indicated by black dashed lines and selected hydrogen bonds illustrated as yellow dashed lines.
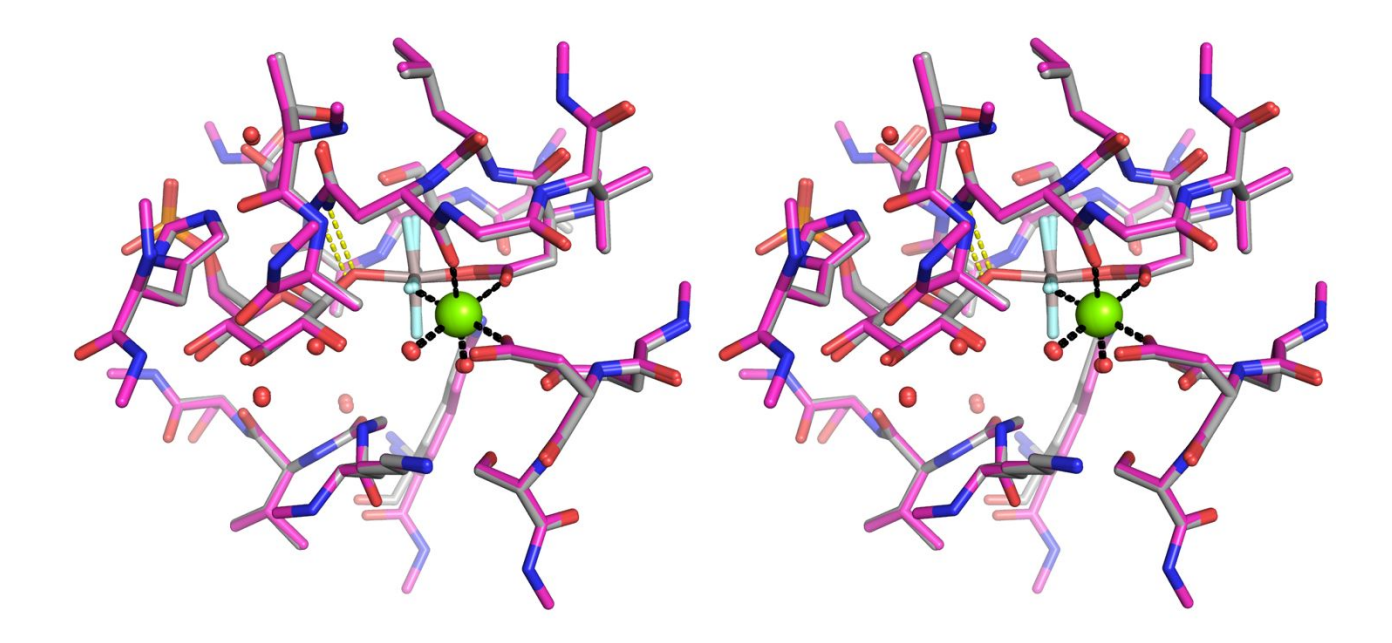
Figure S6. Crosseye stereo representation of QM_{D10N} AlF_4 model (protonated $O1_{G6P}$; magenta carbon atoms) overlaid with βPGM_{D10N}:AlF_4:G6P structure (PDB: 6L03; grey carbon atoms). Standard CPK colouring of non-carbon atoms is used with metal coordination indicated by black dashed lines and selected hydrogen bonds illustrated as yellow dashed lines.
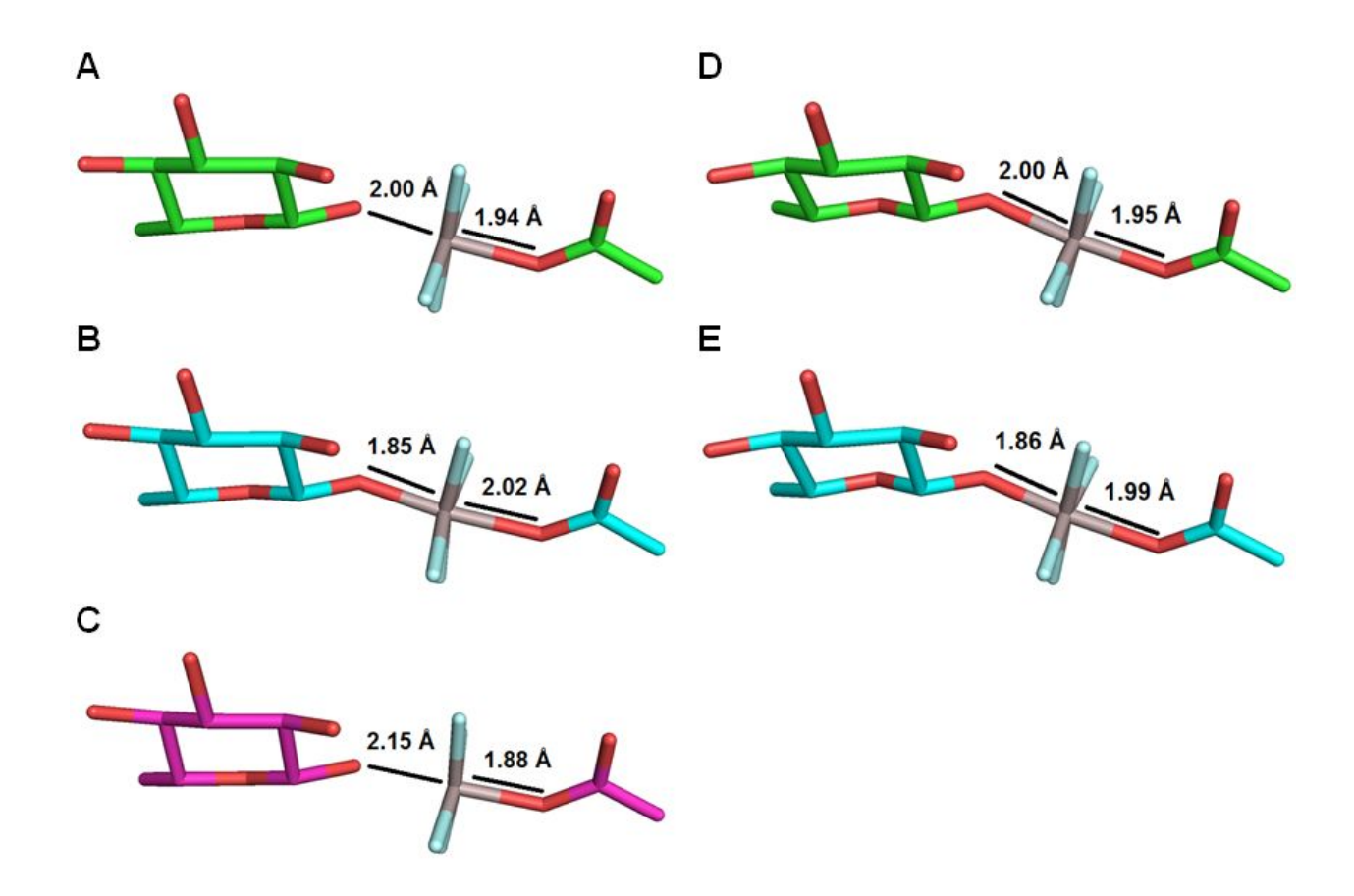
Figure S7. O–P–O Distances in (A) QM_{WT} AlF_4 model, (B) QM_{D10N} AlF_4 model, (C) QM_{D10N} AlF_4 model (protonated $O1_{G6P}$), (D) PDB: 2WF6, and (E) PDB: 6L03.

6. ^{19}F NMR chemical shift calculations

NMR shielding tensors for ^{19}F nuclei in both the βPGM$_{WT}$:AlF$_4$:G6P and βPGM$_{D10N}$:AlF$_4$:G6P active site models were computed from the coupled-perturbed Hartree-Fock equation and gauge-invariant atomic orbitals (GIAO) derived from the DFT electron densities using standard algorithms implemented in GAUSSIAN09.[2] A 6-31+G(d) basis set was used for the fluorine atoms. Calculated shielding tensors were plotted against experimental ^{19}F chemical shift values to determine calculated ^{19}F chemical shift values. See Figure 5 in the main paper for a comparison of calculated and experimental ^{19}F chemical shifts.

7. NMR spectroscopy general methods

$^1H^{15}N$ backbone dynamics and 3D multi-dimensional heteronuclear experiments for dynamic characterisation and resonance assignment of the βPGM_{D10N}:AlF$_4$:G6P complex were acquired at 298 K using 1 mM $^2H^{15}N$ or $^1H^{15}N^{13}C$-labeled substrate-free βPGM_{D10N} in standard NMR buffer (50 mM K+ HEPES (pH 7.2), 5 mM MgCl$_2$, 2 mM NaN$_3$ with 10% (v/v) D$_2$O and 1 mM TSP) containing 5mM AlCl$_3$, 20mM NaF, and 20 mM G6P. Reference ^{19}F spectra for βPGM_{WT} and βPGM_{D10N} AlF$_4$ TSA complexes with either G1P or G6P ligands were acquired at 298 K using 0.5 – 1 mM ^{15}N-βPGM in standard NMR buffer also containing 5 mM AlCl$_3$, 20 mM NaF, 20 mM βG1P/G6P.

8. Backbone assignment of βPGM_{D10N}:AlF_4:G6P complex

The βPGM_{D10N}:AlF_4:G6P complex was generated using 1 mM $^1H^{15}N^{13}C$-labeled βPGM_{D10N} in standard NMR buffer (50 mM K+ HEPES (pH 7.2), 5 mM $MgCl_2$, 2 mM NaN_3 with 10% (v/v) D_2O and 1 mM TSP) with the addition of 5mM $AlCl_3$, 20mM NaF, and 20 mM G6P. Multi-dimensional heteronuclear NMR spectra for backbone resonance assignment of the $^2H,^{15}N,^{13}C$-labeled βPGM_{D10N}:AlF_4:G6P complex were acquired at 298 K on either a Bruker 800 MHz Avance III spectrometer equipped with a TCI cryoprobe and z-axis gradients (MIB) or Bruker 800 MHz Avance spectrometer equipped with a TXI probe and z-axis gradients (Sheffield). The standard suite of $^1H^{15}N$-TROSY and 3D TROSY-based constant time experiments were acquired (HNCO, HN(CA)CO, HNCA, HN(CO)CA, HNCACB, HN(CO)CACB) using non-uniform sampling (NUS) with a multi-dimensional Poisson Gap scheduling strategy with exponential weighting.[14] NUS data were reconstructed using TopSpin3 and multidimensional decomposition.[15] Backbone resonance assignments of the βPGM_{D10N}:AlF_4:G6P complex were obtained using a simulated annealing algorithm employed by the *asstools* assignment program.[16] The backbone assignment is available from the BMRB with accession code (BMRB: 27697).

9. Chemical shift comparisons between WT and D10N AlF$_4$:G6P TSA complexes.
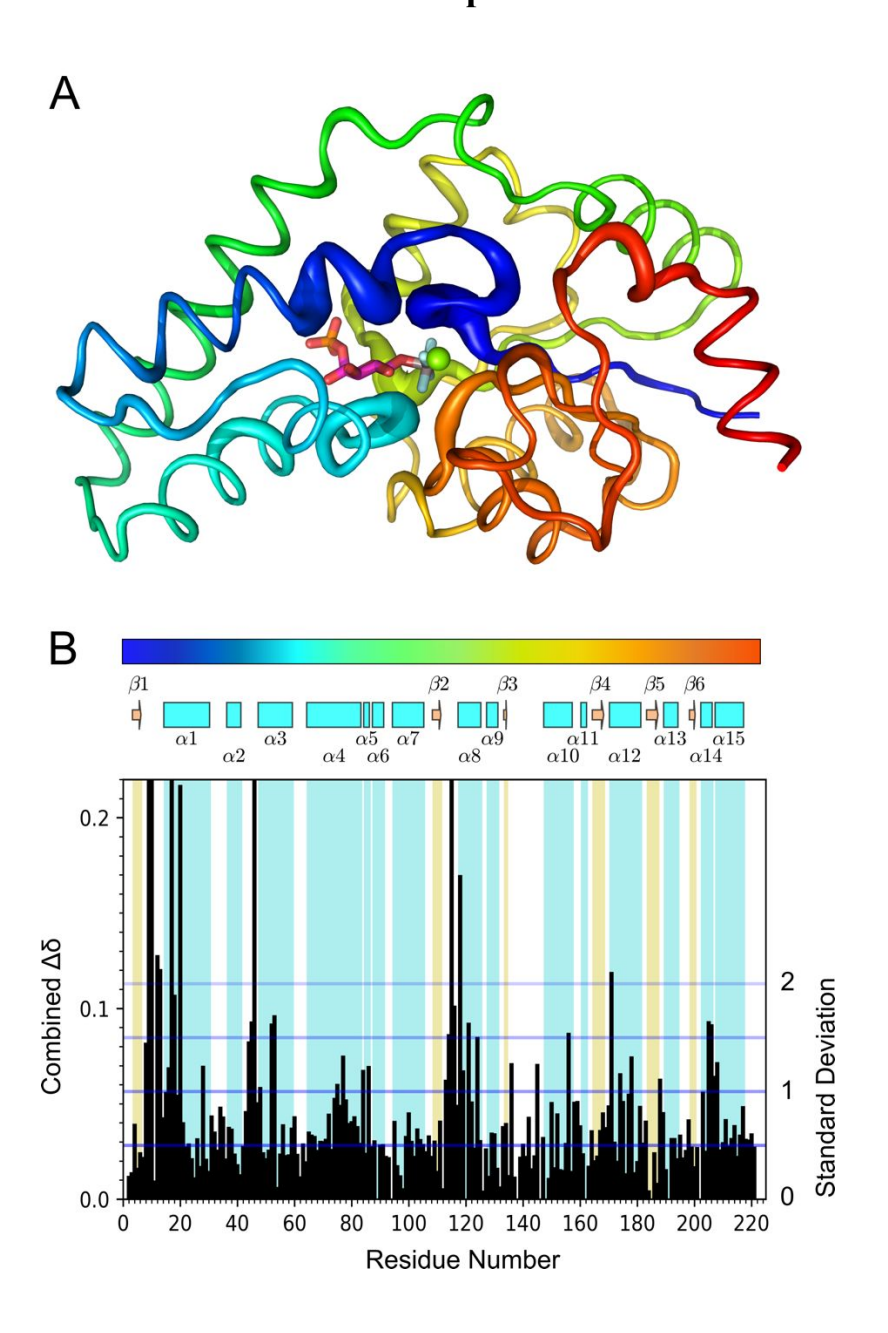
Figure S8. The combined chemical shift differences between the backbone assignments of WT and D10N variants of βPGM complexed with AlF$_4^-$ and G6P. The combined chemical shift was generated using the equation suggested by Williamson[17], with a the alpha scaling factor set to 0.133 to account for the difference in spectral widths of the ^{1}H and ^{15}N dimensions. (A) The magnitude of the combined chemical shift change as a b-factor putty on a crystal structure of the βPGM$_{WT}$:AlF$_4$:G6P complex (PDB: 2WF6 [1]) structure, with the polypeptide chain coloured from blue to red (N-term to C-term) and with the G6P ligand represented as pink sticks. (B) The magnitude of the combined chemical shift difference between the two complexes by residue, with secondary structure indicated and a colour bar that refers to the colouring of the structure in (A).

10. Comparison of Cβ chemical shift of aspartates in βPGM complexes

Table S8. Cβ carbon chemical shifts for all of the assigned aspartate residues in several βPGM complexes, both open (BeF$_3^-$ complex [18]) and closed (MgF$_3^-$ and AlF$_4^-$ complexes).[1,19] Residues were ordered by chemical shift in the MgF$_3$:G6P complex.

Complex	WT:BeF$_3$	WT:MgF$_3$:G6P	WT:AlF$_4$:G6P	WT:BeF$_3$:G6P
BMRB ID	17851	7234	15467	17852
Residue:				
10	40.244	38.331	38.444	-
180	38.648	38.771	38.742	38.736
149	38.971	38.976	38.976	38.951
78	39.130	39.238	39.212	39.177
61	39.412	39.444	39.389	39.319
51	39.489	39.476	39.617	39.459
58	39.560	39.502	39.446	39.488
102	39.593	39.561	39.559	39.602
197	39.558	39.650	39.621	39.603
15	43.166	39.855	39.911	41.010
86	40.819	40.733	40.675	40.706
196	41.111	41.085	41.084	41.060
137	41.396	41.259	–	41.356
91	40.935	41.319	41.261	41.129
203	41.524	41.376	41.379	41.482
170	42.545	41.405	41.358	41.764
193	41.815	41.611	41.609	41.633
37	41.697	41.791	41.786	41.801
133	42.371	42.170	42.136	42.184
8	43.163	43.811	44.011	43.285

11. Protein backbone relaxation measurements and model free analysis

NMR Relaxation Measurements on WT:AlF4:G6P and D10N:AlF4:G6P complexes

βPGM_{WT}:AlF$_4$:G6P and βPGM_{D10N}:AlF$_4$:G6P samples for ^{15}N fast timescale relaxation measurements were performed using [2]H[15]N labelled βPGM enzyme in 5 mm Shigemi D$_2$O matched tubes. Sample conditions for βPGM_{WT}:AlF$_4$:G6P complex - 1mM βPGM_{WT} , 2 mM AlCl$_3$, 10 mM NaF, 10 mM G6P, 5 mM MgCl$_2$, 2 mM NaN$_3$, 1 mM TSP. Sample conditions for the βPGM_{D10N}:AlF$_4$:G6P complex were 1 mM βPGM_{D10N} , 5 mM AlCl$_3$, 20 mM NaF, 20 mM G6P, 5 mM MgCl$_2$, 2 mM NaN$_3$ and 1 mM TSP.

Experiments were acquired using a Bruker 600 MHz Avance DRX spectrometer equipped with a 5-mm TXI cryoprobe and z-axis gradients (Sheffield), a Bruker 800 MHz Avance spectrometer equipped with a 5-mm TXI probe and z-axis gradients (Sheffield), and for the βPGM_{D10N}:AlF$_4$:G6P complex an additional data series using a 950 MHz Avance III spectrometer equipped with a TCI probe and z-axis gradients (Sir Francis Crick Institute, London).

Spin-lattice ^{15}N relaxation rates (R1), rotating frame ^{15}N relaxation rates (R1ρ) and heteronuclear steady-state [15]N-[^{1}H] NOE (hNOE) values were obtained using interleaved TROSY-readout pulse sequences.[20] Temperature compensation was applied in the R1 experiment by incorporating a spin-lock pulse placed off resonance in the inter-scan delay, equal to the longest spin-lock time and the RF power of the R1ρ experiment. Relaxation delays of 0, 80, 240, 400, 400, 640, 800, 1200, 1760, and 2400 ms were used to calculate R1, and delays of 1, 20, 20, 30, 40, 60, 90, 110, 150, and 200 ms were used to calculate R1ρ at 600 MHz and 800 MHz for both complexes. Relaxation delays of 20, 40, 80, 240, 400, 640, 800, 1200, 1200, 1760, 2400, 3200, 4800, 6400, ms were used to calculate R1, and delays of 1, 5, 5, 10, 15, 20, 20, 40, 60, 90, 110, 140, 160, 200 ms were used to calculate R1ρ for the βPGM_{D10N}:AlF$_4$:G6P at 950MHz. The inter scan delay was 3.5 s and the strength of the RF spin-lock field during R1ρ measurement was 1400 Hz at 600 MHz, 1866.7 at 800 MHz and 1500 Hz at 950 MHz. For the hNOE measurement, two interleaved experiments were acquired with relaxation delays of 10s.

Experiments were processed in NMRPipe using a squared sine bell window function, without linear prediction in either dimension.[21] R1 and R2 values were determined in PINT by fitting the integral of the assigned peak to a decaying exponential function across the relaxation series.[22] R2 values were calculated in PINT from fitted R1 values. hNOE values were also fitted in PINT by calculating the difference in peak integral between saturated and unsaturated spectra.

Model free analysis

Model free analysis [23-28] was performed using *relax*.[29-33] R1, R1ρ, and hNOE values at 600 MHz and 800 MHz were used for the βPGM$_{WT}$:AlF$_4$:G6P complex with backbone amide coordinate geometry provided by a crystal structure of the βPGM$_{WT}$:AlF$_4$:G6P complex (PDB: 2WF6 [19]). R1, R1ρ, and hNOE values at 600 MHz and 800 MHz, and 950 MHz were used for the βPGM$_{D10N}$:AlF$_4$:G6P complex with backbone amide coordinate geometry provided by a crystal structure of the βPGM$_{D10N}$:AlF$_4$:G6P (PDB: 5OK2 [7]). Model free analysis was performed in *relax* using models m0-m5 in both complexes (i.e. without using the extended MF formula presented by Clore[34]), however the three terminal residues were excluded due to their absence in both crystal structures. The resulting ellipsoidal diffusion tensors closely matched the geometry of the input crystal structures.

βPGM_WT:AlF_4:G6P complex model free parameters

Residue	Model	S2	S2f	te < 100 or tf	te > 100 or ts	Rex (800.343762 MHz)
				ps	ps	s^-1
1						
2						
3	m1	0.826±0.003				
4	m3	0.845±0.002				2.442±0.152
5	m3	0.831±0.002				1.006±0.136
6	m3	0.829±0.002				2.648±0.092
7	m3	0.814±0.002				1.635±0.094
8	m3	0.826±0.003				3.116±0.111
9	m3	0.857±0.004				2.391±0.213
10	m3	0.842±0.008				5.007±0.349
11	m1	0.882±0.002				
12	m3	0.845±0.002				1.886±0.221
13	m4	0.801±0.005		2.02±0.79		1.370±0.248
14	m3	0.862±0.002				1.027±0.144
15	m4	0.788±0.002		24.35±0.65		0.891±0.093
16	m4	0.801±0.002		8.87±0.71		3.094±0.131
17	m4	0.890±0.002		13.97±1.36		2.448±0.165
18	m4	0.852±0.005		9.20±1.15		1.417±0.272
19						
20	m4	0.895±0.029		7.39±4.09		1.247±0.735
21	m3	0.835±0.001				2.838±0.096
22	m3	0.822±0.001				4.407±0.093
23	m3	0.848±0.001				4.255±0.102
24	m3	0.820±0.001				4.210±0.070
25	m3	0.832±0.002				4.760±0.145
26	m4	0.829±0.002		1.71±0.89		0.620±0.152
27						
28	m3	0.732±0.001				11.036±0.082
29						
30	m4	0.734±0.001		3.68±0.57		6.054±0.382
31	m4	0.795±0.002		4.13±0.71		2.770±0.131
32	m5	0.791±0.004	0.841±0.003		1233.13±69.43	
33	m2	0.821±0.002		7.90±0.93		
34	m5	0.769±0.011	0.817±0.010		1113.52±162.00	
35	m5	0.458±0.009	0.736±0.010		1628.99±26.65	
36	m4	0.837±0.002		5.50±0.92		0.851±0.137
37	m4	0.768±0.001		6.16±0.64		0.985±0.060
38	m4	0.845±0.019		2.77±1.30		1.011±0.678
39	m4	0.809±0.002		10.75±0.76		1.028±0.125
40	m3	0.871±0.002				1.563±0.138
41	m4	0.850±0.002		3.59±1.16		2.029±0.120
42	m3	0.785±0.002				5.736±0.140
43	m3	0.834±0.001				1.960±0.107
44	m4	0.818±0.002		6.28±0.93		1.068±0.132
45	m4	0.810±0.002		4.43±0.93		2.004±0.098
46	m2	0.851±0.002		4.08±1.09		
47	m4	0.801±0.001		5.47±0.82		2.715±0.069
48	m5	0.837±0.003	0.859±0.002		610.85±61.02	
49	m4	0.850±0.002		5.09±1.22		3.159±0.124
50	m4	0.814±0.002		4.83±0.89		2.454±0.117
51	m4	0.825±0.001		5.94±0.87		1.917±0.190
52	m4	0.854±0.002		2.55±1.21		1.175±0.169
53	m3	0.825±0.002				4.081±0.090
54	m4	0.842±0.001		1.80±1.05		2.593±0.092

Residue	Model	S2	S2f	te < 100 or tf	te > 100 or ts	Rex (800.343762 MHz)
				ps	ps	s^-1
55	m3	0.836±0.001				2.723±0.086
56	m3	0.835±0.002				2.176±0.104
57	m3	0.825±0.002				3.936±0.122
58	m4	0.842±0.003		2.67±1.04		2.420±0.122
59	m2	0.880±0.002		6.32±1.38		
60	m4	0.800±0.002		3.55±0.84		1.927±0.104
61	m5	0.718±0.009	0.789±0.007		1053.73±45.18	
62	m5	0.821±0.002	0.846±0.002		409.12±39.37	
63	m5	0.785±0.002	0.824±0.003		403.44±55.39	
64	m5	0.733±0.001	0.772±0.002		206.41±23.03	
65	m4	0.835±0.002		7.05±0.94		0.733±0.097
66	m2	0.873±0.011		6.47±1.57		
67	m2	0.856±0.004		3.99±1.15		
68	m2	0.854±0.002		5.28±1.16		
69	m4	0.833±0.001		2.67±1.06		2.593±0.087
70	m4	0.821±0.002		2.37±0.92		1.775±0.070
71	m4	0.850±0.002		3.06±1.06		1.396±0.104
72	m3	0.860±0.001				0.206±0.129
73	m3	0.837±0.002				3.105±0.152
74	m4	0.843±0.002		2.23±1.08		1.747±0.161
75	m4	0.853±0.002		5.90±1.12		0.596±0.191
76	m3	0.863±0.002				1.126±0.102
77	m3	0.861±0.001				2.342±0.124
78	m5	0.836±0.002	0.850±0.002		793.29±122.02	
79	m2	0.869±0.002		2.10±1.26		
80	m4	0.828±0.002		1.59±1.00		2.757±0.118
81	m3	0.863±0.001				1.362±0.095
82	m4	0.854±0.002		2.70±1.14		1.409±0.121
83	m5	0.834±0.003	0.847±0.005		512.86±111.53	
84	m4	0.772±0.001		11.66±0.62		3.396±0.140
85	m4	0.859±0.002		12.34±0.97		1.445±0.117
86	m5	0.760±0.002	0.844±0.002		894.30±23.80	
87	m4	0.825±0.002		14.77±0.80		1.635±0.092
88	m4	0.835±0.001		6.35±1.04		2.396±0.078
89						
90	m1	0.867±0.007				
91	m4	0.810±0.001		3.64±0.95		1.923±0.107
92	m3	0.875±0.002				2.227±0.102
93	m3	0.889±0.004				1.863±0.141
94						
95	m4	0.831±0.016		16.51±2.20		3.681±0.552
96	m4	0.838±0.002		2.31±0.97		3.429±0.097
97	m3	0.863±0.001				2.182±0.102
98	m3	0.812±0.002				5.021±0.178
99	m3	0.840±0.001				2.543±0.179
100	m3	0.862±0.002				1.124±0.127
101	m3	0.839±0.002				2.280±0.097
102	m3	0.830±0.002				3.398±0.087
103	m3	0.853±0.003				2.720±0.132
104	m3	0.853±0.001				1.268±0.102
105						
106	m1	0.871±0.002				
107	m4	0.867±0.002		3.63±1.36		0.445±0.149
108	m4	0.829±0.002		2.14±0.99		1.347±0.130
109	m3	0.838±0.001				1.822±0.069

Residue	Model	S2	S2f	te < 100 or tf ps	te > 100 or ts ps	Rex (800.343762 MHz) s^-1
110	m3	0.778±0.001				2.386±0.080
111	m3	0.844±0.002				3.820±0.097
112	m3	0.826±0.002				2.776±0.084
113	m3	0.837±0.001				3.083±0.096
114	m3	0.817±0.001				2.131±0.122
115	m0					
116	m3	0.844±0.002				2.367±0.198
117						
118	m2	0.851±0.003		4.67±1.14		
119	m3	0.849±0.002				2.247±0.131
120						
121	m3	0.839±0.005				0.861±0.186
122	m3	0.865±0.003				1.143±0.142
123	m3	0.827±0.002				3.388±0.138
124	m3	0.851±0.002				2.008±0.107
125						
126	m4	0.813±0.003		2.55±0.91		1.173±0.137
127	m4	0.854±0.003		4.43±1.09		2.074±0.167
128	m3	0.807±0.002				4.098±0.133
129	m5	0.856±0.003	0.878±0.003		732.07±94.45	
130	m2	0.853±0.013		8.02±1.34		
131	m4	0.822±0.002		1.60±0.89		3.416±0.106
132	m4	0.822±0.001		3.92±0.90		0.876±0.087
133	m3	0.834±0.002				0.424±0.086
134	m3	0.801±0.002				1.760±0.086
135	m4	0.801±0.004		1.65±0.85		0.625±0.137
136	m3	0.876±0.002				1.062±0.084
137	m4	0.748±0.002		8.05±0.55		1.824±0.080
138						
139	m4	0.760±0.012		4.45±0.87		5.921±0.471
140	m4	0.775±0.002		11.65±0.63		0.464±0.095
141	m5	0.658±0.001	0.765±0.001		537.22±6.02	
142	m5	0.575±0.002	0.803±0.005		842.29±9.49	
143	m5	0.619±0.001	0.738±0.001		497.35±4.22	
144	m2	0.799±0.003		9.92±0.71		
145	m5	0.839±0.003	0.874±0.002		517.74±33.52	
146						
147	m3	0.916±0.001				2.587±0.091
148						
149	m3	0.898±0.001				0.868±0.064
150	m3	0.813±0.001				3.668±0.168
151	m5	0.794±0.008	0.828±0.006		645.36±68.00	
152	m3	0.803±0.002				3.911±0.132
153	m3	0.855±0.009				1.925±0.333
154	m3	0.842±0.002				2.605±0.138
155	m3	0.813±0.002				3.738±0.139
156						
157	m3	0.816±0.002				4.199±0.226
158	m3	0.810±0.002				1.682±0.141
159	m4	0.822±0.003		1.50±0.81		3.266±0.213
160	m3	0.834±0.002				2.644±0.089
161	m4	0.802±0.002		5.57±0.68		3.771±0.128
162						
163	m2	0.831±0.003		14.07±1.07		

Residue	Model	S2	S2f	te < 100 or tf	te > 100 or ts	Rex (800.343762 MHz)
				ps	ps	s^-1
164	m4	0.801±0.002		1.76±0.76		3.683±0.131
165	m3	0.847±0.002				0.833±0.150
166	m3	0.886±0.004				2.891±0.190
167	m3	0.833±0.003				1.572±0.116
168	m3	0.850±0.002				1.478±0.083
169	m3	0.809±0.002				3.461±0.087
170	m4	0.810±0.002		1.65±0.90		1.102±0.116
171	m4	0.880±0.003		3.64±1.50		1.649±0.277
172	m4	0.840±0.002		2.08±0.99		2.080±0.134
173	m3	0.908±0.015				0.812±0.456
174	m3	0.857±0.003				1.661±0.131
175	m5	0.776±0.002	0.817±0.003		883.51±72.78	
176	m3	0.864±0.002				1.945±0.130
177	m3	0.855±0.002				2.427±0.080
178	m3	0.816±0.001				3.520±0.123
179	m3	0.854±0.004				2.586±0.311
180	m3	0.846±0.002				1.539±0.140
181	m3	0.827±0.002				0.808±0.170
182	m3	0.806±0.001				3.549±0.185
183	m3	0.838±0.004				4.281±0.233
184						
185						
186	m3	0.816±0.002				0.990±0.101
187	m3	0.837±0.001				2.408±0.082
188	m3	0.859±0.002				1.979±0.096
189	m3	0.832±0.002				2.478±0.140
190	m4	0.811±0.001		5.21±0.76		1.161±0.059
191						
192	m2	0.851±0.002		7.30±1.18		
193	m4	0.806±0.002		7.19±0.78		2.618±0.152
194	m2	0.813±0.002		5.82±0.84		
195	m4	0.814±0.002		10.10±0.85		1.024±0.090
196	m5	0.726±0.002	0.769±0.002		437.06±27.10	
197	m5	0.851±0.003	0.875±0.003		578.13±72.73	
198	m5	0.715±0.002	0.744±0.001		469.13±30.97	
199	m4	0.837±0.002		7.65±1.06		0.747±0.103
200	m4	0.821±0.001		2.96±0.97		1.898±0.069
201	m4	0.823±0.001		3.57±0.87		2.381±0.075
202						
203	m4	0.810±0.001		3.13±0.77		2.929±0.080
204	m4	0.821±0.002		3.17±0.93		2.253±0.097
205	m4	0.870±0.002		3.78±1.36		3.957±0.207
206	m3	0.843±0.002				5.119±0.137
207	m5	0.866±0.002	0.879±0.009		372.52±104.61	
208	m4	0.724±0.001		2.03±0.58		2.742±0.059
209	m3	0.863±0.001				0.575±0.074
210	m4	0.837±0.002		2.37±1.04		0.737±0.078
211	m2	0.873±0.002		5.51±1.40		
212	m1	0.886±0.002				
213	m3	0.829±0.001				1.518±0.102
214	m5	0.822±0.005	0.838±0.004		1164.56±219.9	
215	m2	0.863±0.001		5.11±1.18		
216	m3	0.877±0.008				1.122±0.362
217	m5	0.790±0.010	0.831±0.007		1429.17±140.7	
218	m5	0.826±0.003	0.856±0.002		582.74±45.14	

βPGM$_{D10N}$:AlF$_4$:G6P complex model free parameters

Residue	Model	S2	S2f	te < 100 or tf ps	te > 100 or ts ps	Rex (950.454467115 MHz) s^{-1}
1						
2						
3	m2	0.788±0.004		2.89±0.58		
4	m3	0.837±0.005				1.940±0.225
5	m2	0.803±0.003		3.38±0.64		
6	m1	0.812±0.002				
7	m4	0.797±0.003		1.39±0.62		0.805±0.161
8	m1	0.831±0.002				
9						
10						
11	m1	0.848±0.003				
12	m2	0.832±0.004		1.16±0.70		
13	m2	0.779±0.004		2.17±0.52		
14	m4	0.823±0.004		6.72±0.77		0.681±0.181
15	m5	0.747±0.002	0.787±0.002		280.51±23.69	
16	m5	0.740±0.003	0.778±0.003		321.41±27.88	
17	m5	0.878±0.003	0.891±0.006		252.88±89.21	
18	m5	0.795±0.007	0.827±0.006		1102.05±115.37	
19	m4	0.757±0.002		4.14±0.43		2.320±0.153
20	m4	0.806±0.004		6.54±0.57		2.525±0.298
21	m4	0.810±0.002		2.15±0.59		0.753±0.161
22	m2	0.835±0.002		3.58±0.66		
23	m4	0.811±0.002		2.06±0.59		1.788±0.196
24	m4	0.815±0.003		3.35±0.62		1.504±0.165
25	m4	0.801±0.003		0.91±0.56		5.088±0.191
26	m2	0.803±0.002		4.51±0.55		
27	m3	0.810±0.004				1.266±0.244
28	m3	0.799±0.003				2.613±0.218
29	m4	0.786±0.003		2.41±0.50		2.313±0.204
30	m4	0.781±0.004		6.99±0.49		1.763±0.365
31	m2	0.775±0.002		5.26±0.44		
32	m5	0.731±0.004	0.793±0.003		1101.91±42.02	
33	m5	0.736±0.006	0.779±0.004		846.77±53.38	
34	m5	0.768±0.010	0.799±0.011		438.74±94.99	
35	m5	0.460±0.007	0.555±0.010		763.39±40.07	
36	m4	0.813±0.002		7.28±0.60		0.443±0.143
37	m2	0.740±0.001		5.92±0.40		
38	m5	0.861±0.007	0.876±0.010		352.68±199.18	
39	m5	0.790±0.003	0.810±0.002		338.20±56.89	
40	m1	0.843±0.002				
41	m2	0.827±0.001		2.16±0.75		
42						
43	m2	0.828±0.003		3.76±0.72		
44	m4	0.802±0.004		5.55±0.63		0.383±0.188
45	m4	0.788±0.003		6.32±0.55		0.768±0.174
46	m1	0.824±0.004				
47	m2	0.811±0.002		6.89±0.64		
48	m5	0.802±0.004	0.825±0.003		439.94±57.87	
49	m4	0.849±0.003		7.09±0.84		0.865±0.217
50	m2	0.807±0.001		6.67±0.58		
51	m2	0.823±0.004		3.43±0.67		
52						
53	m4	0.822±0.003		1.83±0.72		1.510±0.143
54	m2	0.833±0.002		2.41±0.71		
55	m1	0.828±0.003				

Residue	Model	S2	S2f	te < 100 or tf	te > 100 or ts	Rex (950.454467115 MHz)
				ps	ps	s^{-1}
56	m2	0.807±0.003		1.93±0.64		
57	m4	0.824±0.004		2.61±0.66		1.209±0.194
58	m4	0.819±0.004		2.78±0.67		1.985±0.227
59	m4	0.849±0.003		7.28±0.81		0.912±0.139
60	m4	0.778±0.004		7.37±0.55		1.484±0.203
61	m5	0.743±0.010	0.815±0.008		579.43±29.20	
62	m5	0.776±0.004	0.807±0.002		440.30±38.48	
63	m5	0.747±0.002	0.791±0.003		329.08±28.92	
64	m5	0.695±0.002	0.744±0.002		254.29±13.99	
65	m2	0.801±0.002		9.89±0.79		
66	m4	0.826±0.033		3.61±1.13		1.712±1.062
67	m2	0.811±0.004		6.13±0.60		
68	m2	0.813±0.003		6.82±0.66		
69						
70	m5	0.710±0.010	0.779±0.003		6739.16±2140.12	
71						
72	m4	0.819±0.001		3.20±0.69		0.841±0.191
73	m4	0.823±0.003		3.14±0.72		3.043±0.144
74	m4	0.819±0.004		3.08±0.66		0.909±0.195
75	m2	0.814±0.004		7.80±0.65		
76	m3	0.841±0.004				1.783±0.191
77	m2	0.859±0.002		1.45±0.87		
78	m2	0.778±0.002		7.60±0.76		
79	m4	0.842±0.004		4.46±0.85		0.278±0.169
80	m4	0.801±0.004		5.73±0.63		1.766±0.216
81	m2	0.852±0.003		4.19±0.86		
82	m4	0.843±0.004		1.60±0.79		0.524±0.164
83						
84	m5	0.762±0.004	0.790±0.004		200.14±36.84	
85	m2	0.832±0.002		9.42±0.68		
86	m5	0.696±0.002	0.787±0.003		867.20±20.31	
87	m4	0.794±0.002		12.12±0.53		1.011±0.104
88	m2	0.829±0.002		5.22±0.75		
89						
90	m2	0.851±0.009		6.31±0.99		
91	m2	0.806±0.003		4.43±0.62		
92						
93	m2	0.847±0.003		3.88±0.94		
94						
95	m5	0.913±0.007	0.957±0.007		365.26±52.89	
96	m3	0.821±0.002				1.664±0.130
97	m1	0.844±0.004				
98	m3	0.805±0.008				3.015±0.399
99						
100	m2	0.843±0.002		1.50±0.77		
101	m4	0.813±0.002		1.97±0.70		0.702±0.186
102	m3	0.820±0.003				0.995±0.147
103	m3	0.830±0.003				1.130±0.184
104	m3	0.786±0.003				3.303±0.193
105						
106	m2	0.834±0.002		3.95±0.65		
107	m2	0.836±0.002		6.06±0.79		
108	m2	0.762±0.007		4.73±0.56		
109	m2	0.827±0.002		2.79±0.72		
110	m2	0.772±0.001		1.64±0.51		

Residue	Model	S2	S2f	te < 100 or tf	te > 100 or ts	Rex (950.454467115 MHz)
				ps	ps	s⁻¹
111	m1	0.845±0.003				
112	m3	0.811±0.002				0.391±0.093
113	m2	0.811±0.002		3.28±0.69		
114	m1	0.806±0.002				
115						
116	m4	0.805±0.002		3.27±0.58		2.943±0.133
117	m2	0.789±0.003		4.28±0.52		
118	m2	0.822±0.004		2.49±0.71		
119	m2	0.795±0.001		0.96±0.55		
120						
121	m4	0.810±0.003		3.29±0.62		1.168±0.154
122	m3	0.835±0.003				0.461±0.195
123						
124	m4	0.826±0.004		3.59±0.72		1.045±0.228
125	m4	0.821±0.003		5.59±0.70		1.222±0.231
126	m2	0.781±0.002		3.75±0.52		
127	m2	0.836±0.004		8.60±0.73		
128	m4	0.782±0.003		4.35±0.48		3.201±0.202
129	m2	0.822±0.003		8.64±0.70		
130	m2	0.828±0.014		3.25±0.86		
131	m4	0.804±0.002		4.08±0.55		1.740±0.112
132	m2	0.792±0.002		5.26±0.52		
133	m2	0.790±0.003		1.07±0.55		
134	m1	0.794±0.002				
135	m2	0.760±0.002		1.98±0.54		
136	m2	0.831±0.002		4.09±0.77		
137	m4	0.723±0.002		9.44±0.39		1.118±0.110
138						
139	m4	0.803±0.002		10.86±0.58		1.027±0.137
140	m2	0.753±0.002		9.44±0.44		
141	m5	0.665±0.002	0.768±0.002		385.19±7.69	
142	m5	0.582±0.002	0.675±0.002		323.77±7.14	
143	m5	0.611±0.002	0.725±0.001		357.13±4.61	
144						
145						
146						
147	m2	0.881±0.002		4.37±1.00		
148						
149	m1	0.874±0.002				
150	m3	0.816±0.003				1.582±0.230
151	m4	0.829±0.003		2.85±0.75		1.594±0.318
152	m4	0.779±0.002		3.38±0.52		3.242±0.233
153						
154	m3	0.826±0.003				0.477±0.180
155	m4	0.800±0.004		0.91±0.57		2.119±0.218
156	m4	0.809±0.004		1.95±0.59		0.719±0.196
157	m2	0.827±0.005		5.25±0.73		
158	m1	0.747±0.002				
159	m3	0.790±0.005				1.446±0.244
160	m3	0.798±0.002				1.847±0.202
161	m2	0.810±0.001		5.61±0.55		
162						
163	m2	0.756±0.003		5.38±0.52		
164	m3	0.815±0.003				0.370±0.174
165	m4	0.800±0.005		2.47±0.62		0.650±0.260

Residue	Model	S2	S2f	te < 100 or tf	te > 100 or ts	x (950.454467115 M
				ps	ps	s⁻¹
166						
167	m2	0.803±0.003		1.13±0.58		
168	m1	0.813±0.003				
169	m3	0.808±0.003				0.511±0.120
170	m2	0.780±0.002		0.91±0.53		
171	m2	0.871±0.004		4.78±1.00		
172	m4	0.824±0.004		4.84±0.68		0.764±0.204
173	m4	0.856±0.003		3.52±0.86		0.388±0.175
174	m3	0.828±0.007				0.899±0.279
175	m4	0.818±0.003		2.06±0.65		2.144±0.205
176	m4	0.840±0.004		1.46±0.78		3.154±0.206
177	m3	0.830±0.002				1.349±0.158
178	m3	0.797±0.002				1.862±0.167
179						
180	m2	0.830±0.003		6.36±0.70		
181	m1	0.808±0.004				
182	m4	0.804±0.007		1.71±0.63		0.542±0.319
183	m4	0.825±0.006		2.00±0.61		1.755±0.302
184	m2	0.822±0.002		6.58±0.70		
185						
186	m2	0.793±0.003		1.89±0.58		
187	m1	0.827±0.001				
188	m1	0.848±0.002				
189	m4	0.797±0.003		2.52±0.53		1.161±0.148
190	m2	0.782±0.001		6.29±0.49		
191						
192	m2	0.818±0.003		7.88±0.72		
193	m4	0.785±0.003		3.73±0.53		2.225±0.178
194	m2	0.777±0.002		5.51±0.53		
195	m5	0.733±0.002	0.768±0.002		785.79±42.62	
196	m5	0.700±0.003	0.744±0.003		269.76±21.92	
197	m5	0.798±0.005	0.839±0.003		608.79±36.62	
198	m5	0.657±0.002	0.699±0.002		649.44±21.82	
199	m5	0.778±0.002	0.806±0.002		760.62±49.93	
200	m2	0.818±0.002		3.10±0.68		
201	m2	0.816±0.002		3.88±0.63		
202						
203	m4	0.783±0.003		3.58±0.44		1.860±0.126
204	m2	0.795±0.002		5.47±0.55		
205	m4	0.850±0.003		4.04±0.82		2.060±0.200
206	m4	0.838±0.004		3.31±0.72		2.855±0.246
207						
208	m4	0.715±0.002		3.18±0.38		0.766±0.069
209	m4	0.829±0.002		2.53±0.77		0.193±0.099
210	m5	0.749±0.002	0.791±0.002		2049.27±194.03	
211						
212	m2	0.855±0.003		4.55±0.87		
213	m4	0.802±0.003		1.98±0.63		0.744±0.165
214	m2	0.810±0.003		7.73±0.66		
215	m2	0.823±0.003		7.94±0.69		
216						
217	m5	0.751±0.016	0.811±0.011		894.89±87.55	
218						
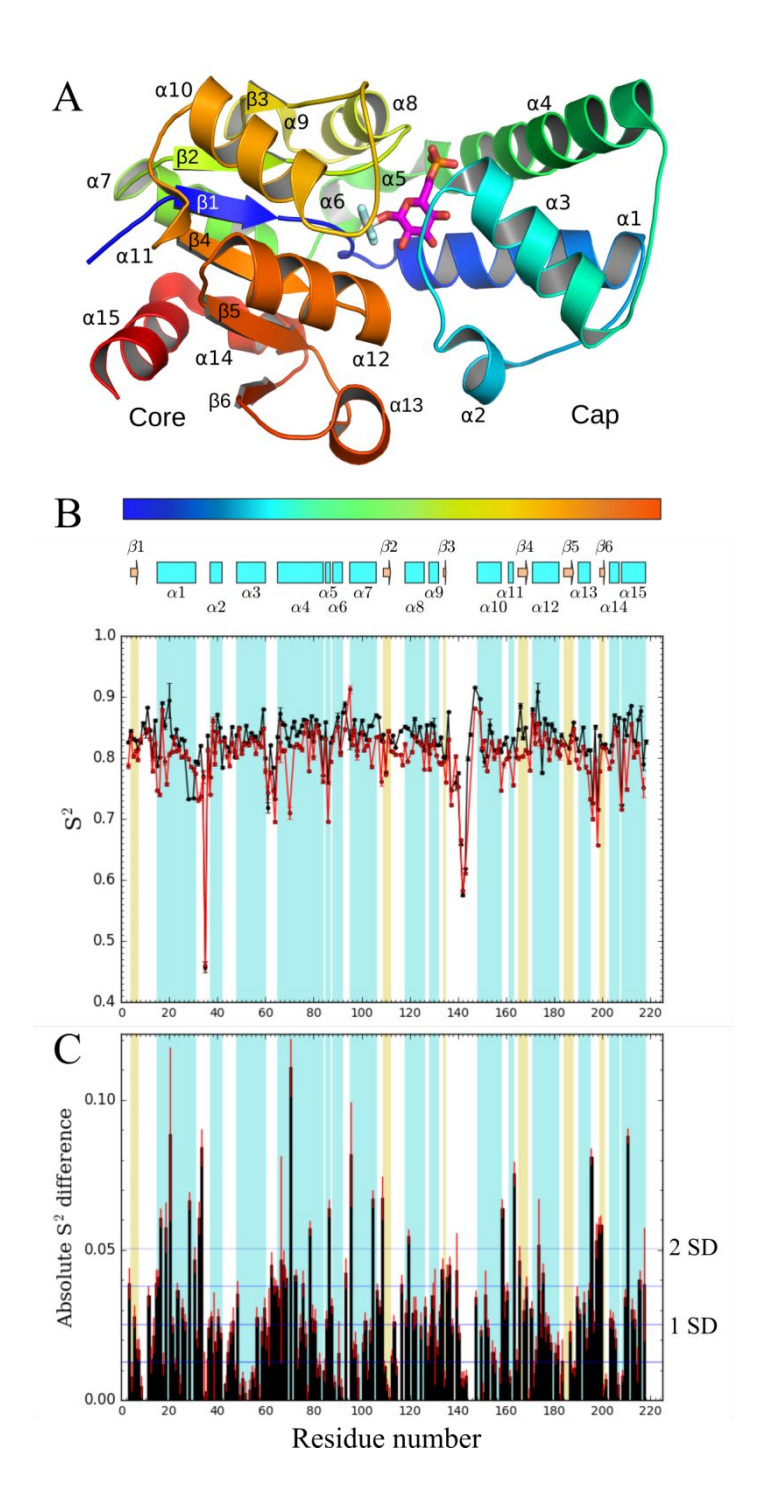
Figure S9. The model free comparison of βPGM_{WT}:AlF_4:G6P and βPGM_{D10N}:AlF_4:G6P complexes. (A) A ribbon representation of the tertiary structure of βPGM (with N- to C-term from blue to red respectively) with α-helices and β-sheets annotated. (B) Order parameters for βPGM_{WT}:AlF:G6P (black) and βPGM_{D10N}:AlF_4:G6P (red) complexes plotted with error (1 standard deviation (SD)). (C) The absolute order parameter difference between βPGM_{WT}:AlF_4:G6P and βPGM_{D10N}:AlF_4:G6P complexes is presented with error bars at 1 SD (red). Horizontal lines correspond to the standard deviations for the dataset.

12. Chemical shift transition towards unfolded state analysis
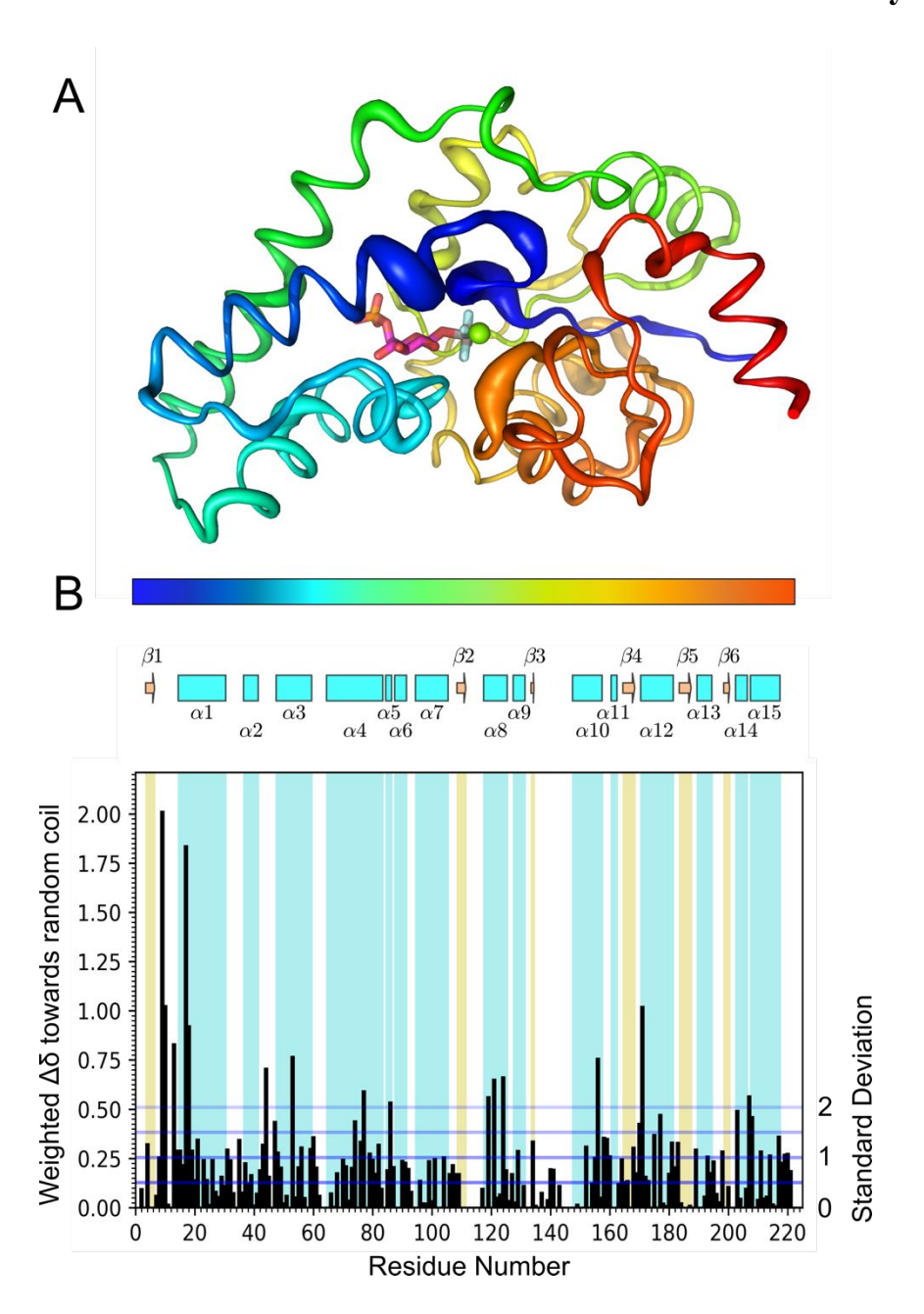
Figure S10. The combined backbone amide chemical shift differences between the assignments of WT and D10N variants of βPGM complexed with AlF_4^- and G6P. Chemical shifts of the βPGM$_{D10N}$:AlF$_4$:G6P complex were compared to both WT and a random coil chemical shift library (without local sequence compensation).[35] If the chemical shift moved towards random coil, the combined chemical shift was reported as in Williamson.[17] Transition to random coil is primarily observed in the active site with large transitions for key residues in the hinge region (I13, A17, G18 and S171). (A) Residues that indicate transition to random coil, between βPGM$_{WT}$:AlF$_4$:G6P and βPGM$_{D10N}$:AlF$_4$:G6P complexes, with the polypeptide chain coloured from blue to red (N-term to C-term), magnitude of combined chemical shift change indicated by b-factor putty, and AlF$_4$ and G6P (pink) ligands included for reference. (B) The absolute value of the chemical shift change towards random coil-like chemical shift per residue with secondary structure indicated and a colour bar that refers to the colouring of the structure in (A). Horizontal lines correspond to the standard deviations for the dataset.
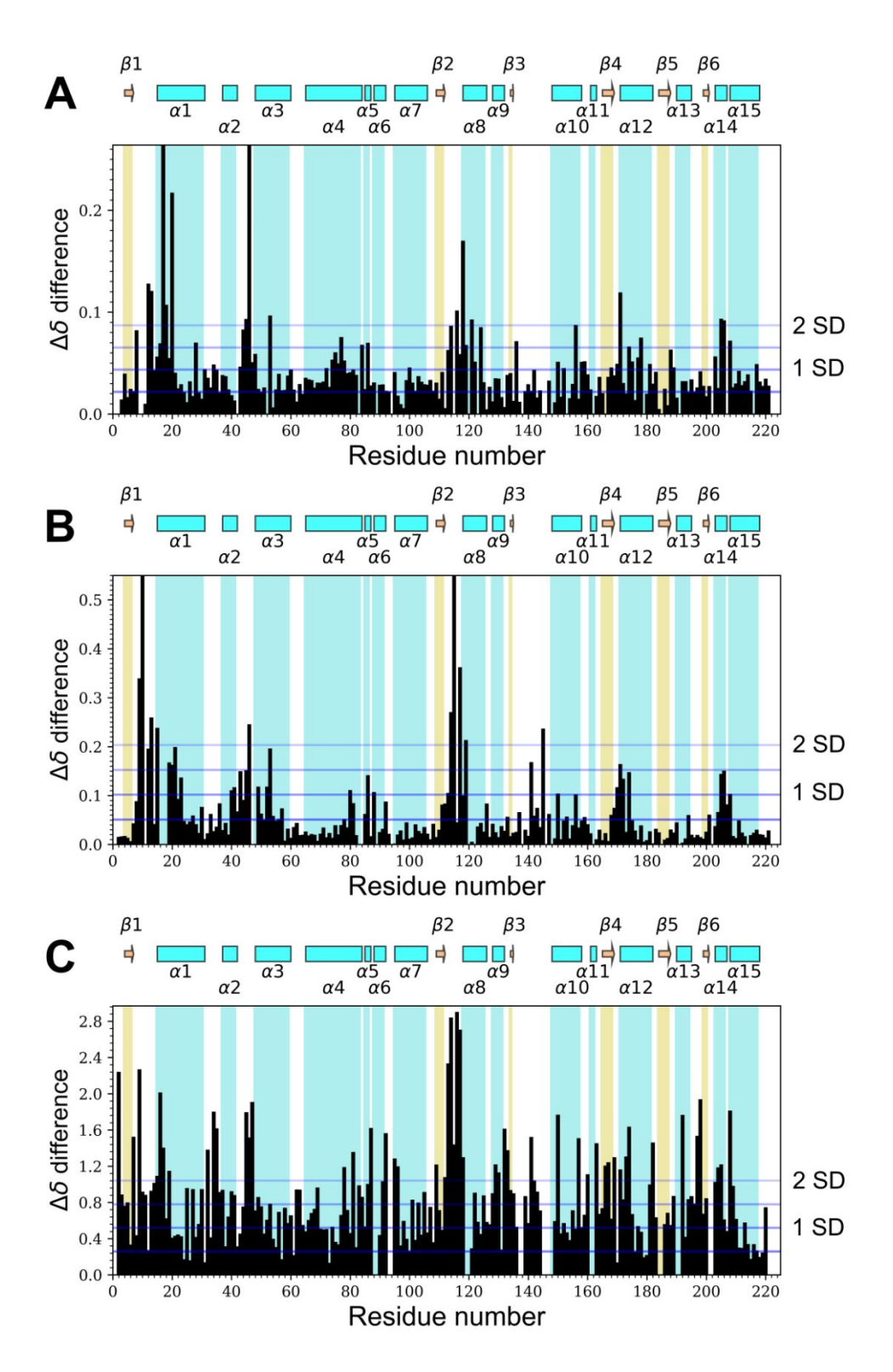
Figure S11. Chemical shift analysis of combined backbone amide (HN and N) chemical shift perturbation. (A) Comparison of βPGM$_{WT}$:AlF$_4$:G6P and βPGM$_{D10N}$:AlF$_4$:G6P complexes, (B) comparison of βPGM$_{WT}$:MgF$_3$:G6P and βPGM$_{WT}$:BeF$_3$:G6P complexes, and (C) comparison of βPGM$_{WT}$:MgF$_3$:G6P and βPGM$_{D10N}$:βG16BP complexes.

13. ^{19}F NMR methods and SIIS determination

1D ^{19}F spectra

One-dimensional ^{19}F spectra to characterise WT and D10N AlF$_4$:G6P TSA complexes were acquired using a Bruker 500MHz Avance III spectrometer equipped with a 5mm QCI-F cryoprobe with z-axis gradients (MIB). A spectral width of 120 ppm centered at -140 ppm for ^{19}F was used without proton decoupling. Spectra were accumulations of 1024 – 2048 transients in order to achieve a sufficient signal-to-noise ratio. Spectra were processed with an EM window function with 10 Hz line-broadening and were analyzed in Topspin (Bruker).

^{19}F spectra of βPGM$_{WT}$ and βPGM$_{D10N}$ AlF$_4$:G6P TSA complexes for initial characterisation were acquired at 298 K using 0.5 – 1 mM ^{15}N-βPGM in standard NMR buffer (50 mM K+ HEPES pH 7.2/7.2*, 5 mM MgCl$_2$, 1 mM TSP). Both βPGM$_{WT}$ and βPGM$_{D10N}$ - AlF$_4$:G6P TSA complexes were made using 5 mM AlCl$_3$, 20 mM NaF, and ca. 20 mM G6P.

Solvent induced isotope shift (SIIS) value determination for WT and D10N complexes

Both βPGM$_{WT}$ - and βPGM$_{D10N}$ - AlF$_4$:G6P complexes were made in H$_2$O and D$_2$O using ^{13}C-1 labelled G6P in attempt to also characterise the chemical environment of the C1 carbon in each of the complexes. The (U)^{13}C1 labelled G6P was synthesized by incubating 45 mM 100% ^{13}C1-glucose with 14 U of hexokinase and ca. 50 mM ATP in a reaction volume of 4 ml, using a buffer of TRIS 100 mM (pH 8), MgCl$_2$ 50 mM, and EDTA 2 mM. The reaction was incubated for 4 hours at which point hexokinase (90 kDa) was removed by passing the reaction mixture through a 10 kDa MWCO vivaspin. The filtrate was split into two equal volumes and each was lyophilized overnight. One (U)^{13}C-1 labelled G6P mix was re-suspended in 100 μl NMR buffer that contained 99.98 % D2O, while the other was suspended in 100 μl NMR buffer in 100% H$_2$O.

WT and D10N protein samples were buffer exchanged into standard NMR buffer with either 100% H$_2$O or 99.9% D$_2$O, and two AlCl$_3$ and NaF stocks were prepared in both 100% H$_2$O and 99.98% D$_2$O. The AlF$_4$:G6P TSA complexes were made using ca. 1 mM WT and D10N ^{15}N-labelled enzyme in either 100% H$_2$O or 99.7% D$_2$O standard NMR buffer, supplemented with 5 mM AlCl$_3$, 20 mM NaF, and 40 mM (U)^{13}C-1 labelled G6P, resulting in 4 samples in total, two 100% H$_2$O and two *ca*. 99% D$_2$O. For H$_2$O samples, a 100% D$_2$O capillary was included to provide frequency lock in the spectrometer. These four samples were then used to record ^{19}F and ^{13}C 1D spectra of each of the complexes with SIIS values determined following the change in chemical shift of fluorine resonances in H$_2$O and in D$_2$O. ^{19}F spectra were accumulations of 2048 transients with a spectral width of 120 ppm centered at -140 ppm, without proton decoupling. Spectra were processed using an EM window function with 10 Hz line-broadening in Topspin (Bruker), and referenced using TopSpin internal referencing.

In the AlF$_4$:G6P TSA complex with D10N two separate complexes were observed. The first of these complexes closely reflected the chemical shifts of βPGM$_{D10N}$:AlF$_4$:G6P TSA complex that was initially assigned. The second complex was more populated at equilibrium, and likely corresponds to the βPGM$_{D10N}$:AlF$_4$:H$_2$O:βG1P that has previously been observed

crystallographically (PDB: 5O6R [7]). The F1 resonance in this complex that coordinates the catalytic Mg ion has moved significantly upfield compared to the F1 resonance in the βPGM_{D10N}:AlF$_4$:G6P TSA complex, which is consistent with the loss of a hydrogen bond from the 2-OH group. This observation is identical to those previously reported using the MgF$_3^-$ TSA and fluoro-phosphonate βG1P analogs which were both crystallised and characterised by NMR previously.[36]
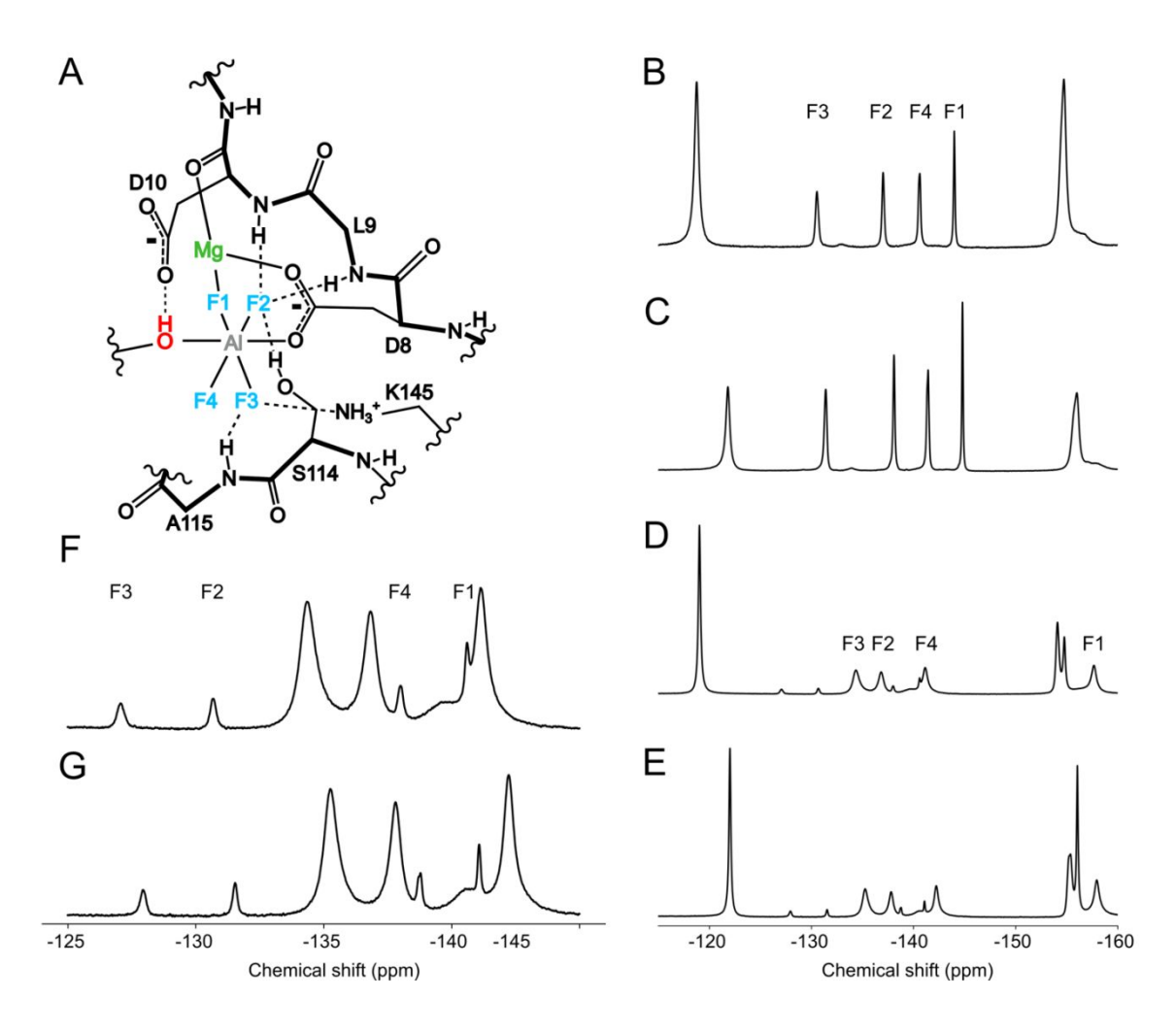
SIIS value determination for WT and D10N AlF$_4$:G6P complexes

Figure S12. 1D ^{19}F NMR spectra of βPGM$_{WT}$ and βPGM$_{D10N}$ complexed with AlF$_4^-$ and G6P/βG1P. (A) Presents a schematic of the active site of βPGM complexed with AlF$_4^-$ (blue and grey atoms), the catalytic Mg^{2+} ion (green) and a nucleophilic hydroxyl group (red) that could belong to the 1-OH or 6-OH of a phosphorylated glucose, or to a water molecule. Backbone bonds are illustrated using thick lines, side chains (and Mg^{2+} coordination) using thin lines, and hydrogen bonds using dashed lines. Fluorine atoms are labelled in accordance with standard IUPAC nomenclature.[37] (B) and (C) correspond to ^{19}F NMR spectra of the βPGM$_{WT}$:AlF$_4$:G6P TSA complex in (B) 100% H$_2$O NMR buffer and (C) 100% D$_2$O NMR buffer. Fluorine resonances are labelled according to the reference scheme in A, with assignments determined previously.[19] (D) and (E) correspond to 1D ^{19}F NMR spectra of a mixed population of βPGM$_{D10N}$:AlF$_4$:H$_2$O:βG1P and βPGM$_{D10N}$:AlF$_4$:G6P TSA complexes, with the βG1P complex being favoured at equilibrium. The βPGM$_{D10N}$:AlF$_4$:H$_2$O:βG1P complex in (D) 100% H$_2$O NMR buffer and (E) 100% D$_2$O NMR buffer is annotated with a transferred assignment, using the upfield shift phenomena observed in Jin *et al.* 2014.[36] (F) and (G) correspond to a magnified view of the βPGM$_{D10N}$:AlF$_4$:G6P TSA complex in the previous NMR spectra, with the complex in (F) 100% H$_2$O NMR buffer and (G) 100% D$_2$O NMR buffer with transferred assignments from the WT complex annotated, which themselves were corroborated by DFT chemical shift prediction. Chemical shifts for (B) and (C) are presented in Table S4, for (D) and (E) are presented in Table S5, and for (F) and (G) are presented in Table S6.

Table S9. The chemical shifts and solvent-induced isotope shifts (SIIS) values for the βPGM$_{WT}$:AlF$_4$:G6P complex. **Sub-tables A** (H$_2$O) and **B** (D$_2$O) correspond to the chemical shifts and peak linewidths at half height (FWHH) for the βPGM$_{WT}$:AlF$_4$:G6P complex illustrated in Figure S12. Linewidth was extracted from the spectra using the deconvolution tool *dcon* in TopSpin v.4.0. **Sub-table C** gives the SIIS (ppm) for each of the fluorine resonances defined as ^{19}F(H$_2$O buffer) – ^{19}F(100% D$_2$O buffer), as well as the change in LWHH which is defined as LWHH(D$_2$O buffer) – LWHH(100% H$_2$O buffer).

A

Fluorine	δ (ppm)	LWHH (Hz)
F1	-144.0	67
F2	-137.0	102
F3	-130.6	139
F4	-140.6	111

B

Fluorine	δ (ppm)	LWHH (Hz)
F1	-144.8	58
F2	-138.1	85
F3	-131.4	123
F4	-141.4	108

C

Fluorine	SIIS (ppm)	ΔLWHH (Hz)
F1	0.8	-10
F2	1.1	-17
F3	0.8	-16
F4	0.8	-3

Table S10. The chemical shifts and solvent-induced isotope shifts (SIIS) values for the βPGM$_{D10N}$:AlF$_4$:G6P complex. **Sub-tables A** (H$_2$O) and **B** (D$_2$O) correspond to the chemical shifts and peak linewidths at half height (FWHH) for the βPGM$_{D10N}$:AlF$_4$:G6P complex illustrated in Figure S12. **Sub-table C** gives the SIIS (ppm) for each of the fluorine resonances defined as ^{19}F(H$_2$O buffer) – ^{19}F(100% D$_2$O buffer), as well as the change in LWHH which is defined as LWHH(D$_2$O buffer) – LWHH(100% H$_2$O buffer).

A

Fluorine	δ (ppm)	LWHH (Hz)
F1	-140.7	274
F2	-130.7	77
F3	-127.1	100
F4	-138.0	186

B

Fluorine	δ (ppm)	LWHH (Hz)
F1	-141.1	198
F2	-131.5	69
F3	-128.0	81
F4	-138.7	168

C

Fluorine	SIIS (ppm)	ΔLWHH (Hz)
F1	0.4	-76
F2	0.9	-7
F3	0.9	-19
F4	0.8	-18

Table S11. The chemical shifts and solvent-induced isotope shifts (SIIS) values for the βPGM$_{D10N}$:AlF$_4$:H$_2$O:βG1P complex. **Sub-tables A** (H$_2$O) and **B** (D$_2$O) correspond to the chemical shifts and peak linewidths at half height (FWHH) for the βPGM$_{D10N}$:AlF$_4$:H$_2$O:βG1P complex illustrated in Figure S12. **Sub-table C** gives the SIIS (ppm) for each of the fluorine resonances defined as δ^{19}F(H$_2$O buffer) – δ^{19}F(100% D$_2$O buffer), as well as the change in LWHH which is defined as LWHH(D$_2$O buffer) – LWHH(100% H$_2$O buffer).

A

Fluorine	δ (ppm)	LWHH (Hz)
F1	-157.6	315
F2	-136.8	291
F3	-134.4	329
F4	-141.1	260

B

Fluorine	δ (ppm)	LWHH (Hz)
F1	-158.0	340
F2	-137.8	246
F3	-135.3	290
F4	-142.2	244

C

Fluorine	SIIS (ppm)	ΔLWHH (Hz)
F1	0.3	25
F2	1.0	-45
F3	0.9	-39
F4	1.1	-16

14. X-ray crystallography methods

Crystallisation and refinement of the βPGM_{D10N}:AlF$_4$:G6P structure was reported previously[7] but subsequent refinement of the βPGM_{D10N}:AlF$_4$:G6P structure with carboxamide of residue N10 in both 180° sidechain rotamers is presented here. Initial refinement with the N10 carboxamide oriented such that the carbonyl atom coordinated the 1-OH group of G6P, resulted in a >3σ difference map peaks for the nitrogen atoms indicating that the incorrect rotamer had been modelled (Figure S5). Reorientation of the carboxamide such that the nitrogen atom coordinates the 1-oxygen atom of G6P (O1$_{G6P}$) and subsequent refinement results in the disappearance of difference map peaks at this position.

Given the energetic penalty associated with deprotonation of the O1$_{G6P}$ atom when coordinated by the NH$_2$ group of N10, it would suggest that a conformer where the 1-OH group is not deprotonated would be preferred. This prediction strongly correlates with the solution NMR data presented in Supporting Information Section 13 (Figure S12), where the βPGM_{D10N}:AlF$_4$:H$_2$O:βG1P complex (PDB: 5O6R [7]) is preferred at equilibrium in a conformation where the N10 sidechain amine coordinates a water molecule, rather than the nucleophilic 1-OH group. In this case, the enzyme preparation has equilibrated G6P with βG1P in the dead-time of the experiment due to residual catalytic activity, which permitted the observation of equilibrium populations of the two complexes.[7]

Refinement of another βPGM_{D10N}:AlF$_4$:G6P crystal at a higher resolution was performed (1.02 Å; PDB: 6L03) to further investigate the nature of the TSA binding. The crystal was both obtained and refined using the methods described previously.[7] This crystal was a *plate* morphology, data collection statistics presented in Table S5. Ligands were omitted until final rounds of refinement to avoid building into biased Fourier maps. In order to satisfy the electron density present, it was necessary to model *ca*. 50 residues across the cap and core domain with split occupancies, with the second occupancy chain translated *ca*. 1 Å away from the first chain. A B-factor weighting of 0.001 was applied in the final stages of refinement to avoid biasing atomic positions to minimise local b-factors. The resulting structure closely reflects the previous structure, and accommodates the ligand in a near identical manner (Figure S6).

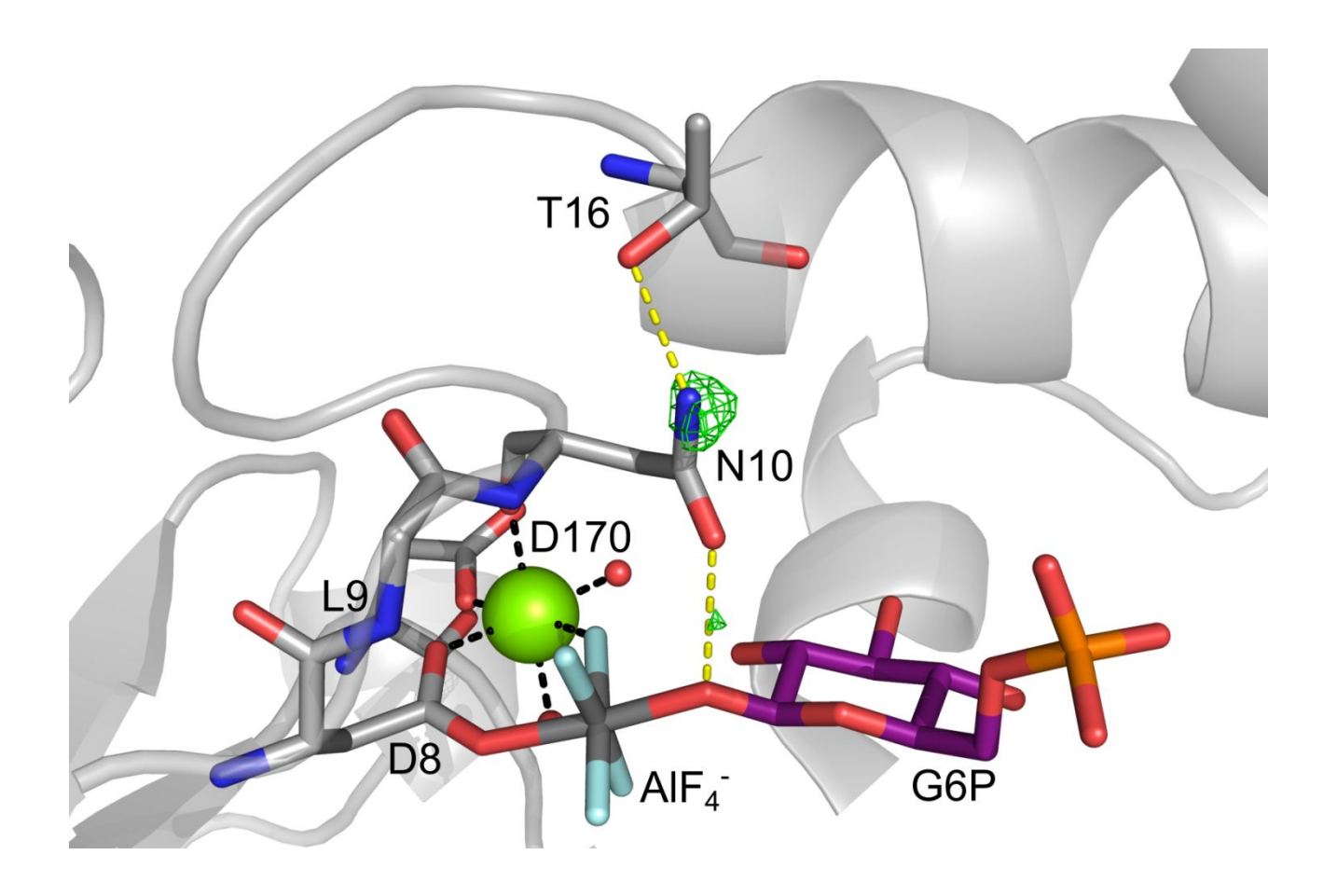## 15. N10 sidechain rotamer indicates deprotonation of G6P 1-OH group

Figure S13. Illustration of the incorrect N10 carboxamide orientation, where the difference density (Fo − Fc; green mesh) for the βPGM$_{D10N}$:ALF$_4$:G6P structure is shown (PDB: 5OK2 [7]). Selected active site residues are shown as sticks in standard CPK colours, with carbons (grey), aluminium (dark grey), fluorine (light blue), and magnesium (light green). The G6P ligand is shown with purple carbon atoms (for clarity) and structural waters are shown as small red spheres. Yellow dashes indicate hydrogen bonds to and from residue N10 and black dashes show metal ion coordination. The difference density was generated following N10 side chain reorientation in the final deposited structure (with subsequent re-refinement against the original data) and is contoured at 3σ.

16. X-ray crystallography data acquisition and refinement table

Table S12. Data acquisition and processing for the new βPGM_{D10N}:AlF$_4$:G6P complex.

Data acquisition	
Complex	βPGM_{D10N}:AlF$_4$:G6P
PDB code	6L03
Wavelength (\AA)	0.97949
Beamline	I02
Facility	DLS
Space group	P2$_1$2$_1$2$_1$
Cell dimensions	
a, b, c, (Å)	37.520, 54.280, 104.420
α, β, γ (°)	90.000, 90.000, 90.000
Resolution (Å)[1]	37.52 – 1.02 (1.02 – 1.05)
R$_{merge}$[1,2]	0.045 (0.917)
R$_{pim}$[1]	0.021 (0.589)
CC-half	0.999 (0.542)
$<I/\sigma I>$[1]	16.1 (1.3)
Completeness (%)[1]	97.6 (82.5)
Multiplicity[1]	6.5 (3.7)
Total reflections	106736
Unique reflections	6606
Molecular replacement model	2WF6

Data refinement	
R (%)[3] / R$_{free}$ (%)[4]	15.15 / 17.47
Protein	1961
Ligands	21
Metal ions	2
Water	232
Protein residues (asterix)	219
RMS deviations:	
Length	0.0072
Angles	1.507
Average B factor (Å^2)	
Main chain	13.581
Side chains	16.464
Ligands (AlF$_4$ then G6P)	11.478, 11.435
Metal Ions (Mg^{2+} then Na$^+$)	10.306, 16.697
Water	23.935
Ramachandran analysis	
Favoured/allowed (\%)	97.65
Disallowed (\%)	0.39
Molprobity score (percentile)	1.27 (88th)

[1]Values for the higher resolution shell are in parenthesis.

[2]$R_{merge} = \Sigma\Sigma|I(h) - I(h)_i|/\Sigma\Sigma I(h)_i$, where I(h) is the mean weighted intensity after rejection of outliers.

[3]$R = \Sigma_{hkl}||F_{obs}| - k|F_{calc}||/\Sigma_{hkl}|F_{obs}|$, where F$_{obs}$ and F$_{calc}$ are the observed and calculated structure factor amplitudes.

[4]$R_{free} = \Sigma_{hkl \subset T}||F_{obs}| - k|F_{calc}||/\Sigma_{hkl \subset T}|F_{obs}|$, where F$_{obs}$ and F$_{calc}$ are the observed and calculated structure factor amplitudes and T is the test set of data omitted from refinement (5% in this case).

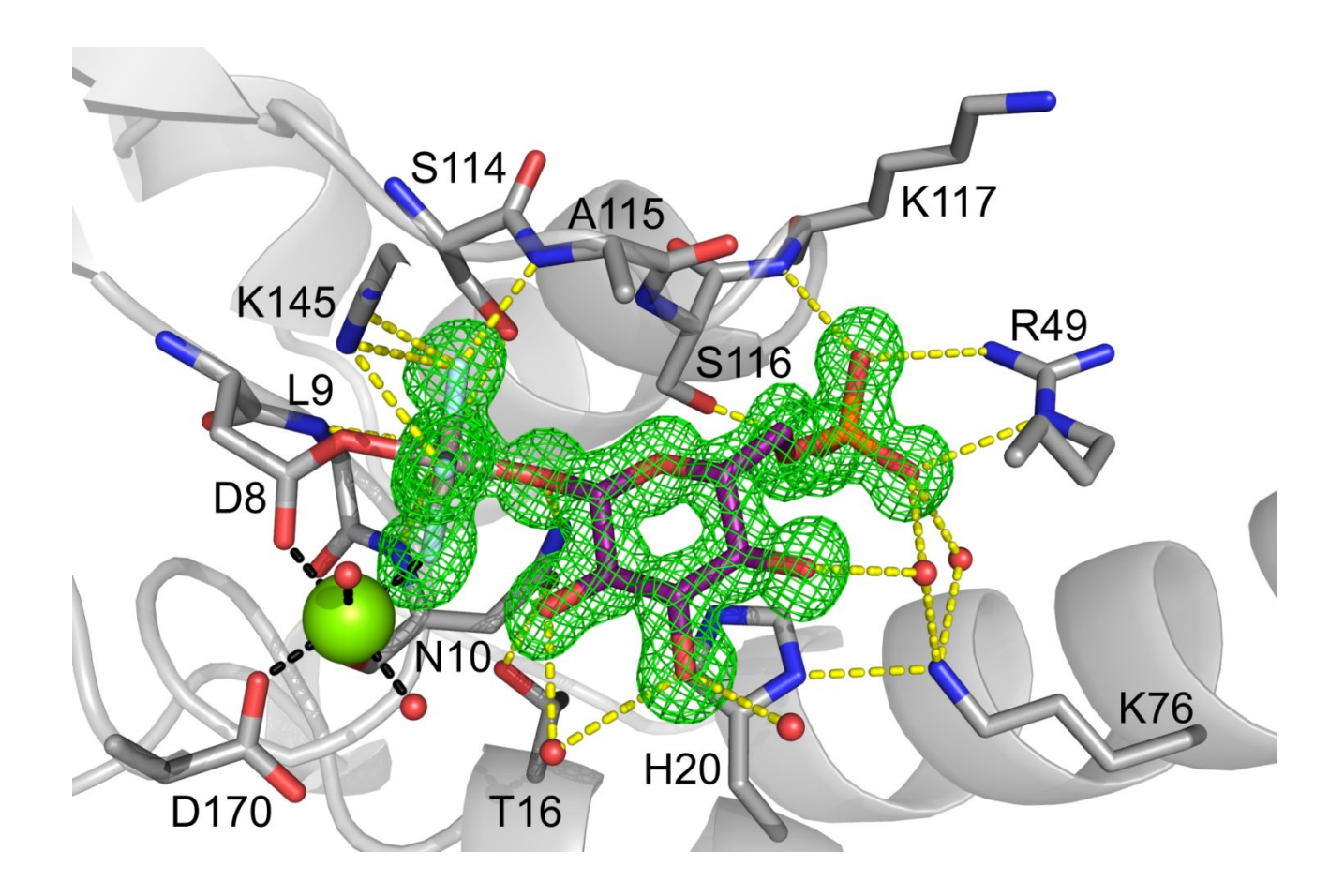# 17. Omit map for βPGM$_{D10N}$:AlF$_4$:G6P complex (PDB: 6L03)

Figure S14. The difference density (Fo – Fc; green mesh) for the βPGM$_{D10N}$:ALF$_4$:G6P structure (PDB: 6L03). Selected active site residues are shown as sticks in standard CPK colours, with carbons (grey), aluminium (dark grey), fluorine (light blue) and magnesium (light green). The G6P ligand is shown with purple carbon atoms (for clarity) and structural waters are shown as small red spheres. Yellow dashes indicate hydrogen bonds and black dashes show metal ion coordination. The difference density was generated following omission of the AlF$_4^-$ and G6P from the final structure (with subsequent re-refinement) and is contoured at 3σ.

18. Table of angles within crystallographically determined AlF$_4^-$ groups

Table S13. F_x-Al-OD1$_{D8}$ and O1$_{G6P}$-Al-F_x angles averaged across the four fluorides in each of the AlF$_4^-$ TSA complexes. Additionally, the improper angle that the Al atom makes to the square plane of the 4 fluorides is reported as an average of all possible planes to account for any asymmetry present. The asterisk in the 2WF6 complex denotes that the angle is of opposite direction to the improper angle reported for PDB: 5OK2 and PDB: 6L03 structures.

PDB:	Oδ1$_{D8}$ – Al – Fx (°)	O1$_{G6P}$ – Al – Fx (°)	Al – F$_{1-4}$ improper angle
2WF6	91.22	88.90	1.70 *
5OK2	89.10	90.97	1.32
6L03	88.00	92.10	2.84

19. References

(1) Baxter, N. J.; Blackburn, G. M.; Marston, J. P.; Hounslow, A. M.; Cliff, M. J.; Bermel, W.; Williams, N. H.; Hollfelder, F.; Wemmer, D. E.; Waltho, J. P. Anionic Charge Is Prioritized over Geometry in Aluminum and Magnesium Fluoride Transition State Analogs of Phosphoryl Transfer Enzymes. *J. Am. Chem. Soc.* **2008**, *130*, 3952.

(2) Frisch, M. J.; Trucks, G. W.; Schlegel, H. B.; Scuseria, G. E.; Robb, M. A.; Cheeseman, J. R.; Scalmani, G.; Barone, V.; Mennucci, B.; Petersson, G. A.; Nakatsuji, H.; Caricato, M.; Li, X.; Hratchian, H. P.; Izmaylov, A. F.; Bloino, J.; Zheng, G.; Sonnenberg, J. L.; Hada, M.; Ehara, M.; Toyota, K.; Fukuda, R.; Hasegawa, J.; Ishida, M.; Nakajima, T.; Honda, Y.; Kitao, O.; Nakai, H.; Vreven, T.; Montgomery, J. A.; Peralta, J. E.; Ogliaro, F.; Bearpark, M.; Heyd, J. J.; Brothers, E.; Kudin, K. N.; Staroverov, V. N.; Kobayashi, R.; Normand, J.; Raghavachari, K.; Rendell, A.; Burant, J. C.; Iyengar, S. S.; Tomasi, J.; Cossi, M.; Rega, N.; Millam, J. M.; Klene, M.; Knox, J. E.; Cross, J. B.; Bakken, V.; Adamo, C.; Jaramillo, J.; Gomperts, R.; Stratmann, R. E.; Yazyev, O.; Austin, A. J.; Cammi, R.; Pomelli, C.; Ochterski, J. W.; Martin, R. L.; Morokuma, K.; Zakrzewski, V. G.; Voth, G. A.; Salvador, P.; Dannenberg, J. J.; Dapprich, S.; Daniels, A. D.; Farkas; Foresman, J. B.; Ortiz, J. V.; Cioslowski, J.; Fox, D. J. Gaussian Inc, Wallingford CT, 2009.

(3) Lee, C.; Yang, W.; Parr, R. G. Development of the Colle-Salvetti correlation-energy formula into a functional of the electron density. *Phys. Rev. B* **1988**, *37*, 785.

(4) Becke, A. D. Density-functional thermochemistry. III. The role of exact exchange. *J. Chem. Phys.* **1993**, *98*, 5648.

(5) Vosko, S. H.; Wilk, L.; Nusair, M. Accurate spin-dependent electron liquid correlation energies for local spin density calculations: a critical analysis. *Can. J. Phys.* **1980**, *58*, 1200.

(6) Stephens, P. J.; Devlin, F. J.; Chabalowski, C. F.; Frisch, M. J. Ab initio calculation of vibrational absorption and circular dichroism spectra using density functional force fields. *J. Phys. Chem.* **1994**, *98*, 11623.

(7) Johnson, L. A.; Robertson, A. J.; Baxter, N. J.; Trevitt, C. R.; Bisson, C.; Jin, Y.; Wood, H. P.; Hounslow, A. M.; Cliff, M. J.; Blackburn, G. M.; Bowler, M. W.; Waltho, J. P. van der Waals Contact between Nucleophile and Transferring Phosphorus Is Insufficient To Achieve Enzyme Transition-State Architecture. *ACS Catal.* **2018**, *8*, 8140.

(8) Popelier, P. L. A., Quantum Chemical Topology. In *The Chemical Bond - 100 years old and getting stronger*, Mingos, M., Ed. Springer: Switzerland, 2016; pp 71-117.

(9) Bader, R.F.W. *Atoms in molecules. A quantum theory.*; Oxford University Press: Oxford, 1990.

(10) Keith, T.; TK Gristmill Software: Overland Park KS, USA, 2017.

(11) Blanco, M. A.; Martín Pendás, A.; Francisco, E. Interacting Quantum Atoms: A Correlated Energy Decomposition Scheme Based on the Quantum Theory of Atoms in Molecules. *J. Chem. Theory Comput.* **2005**, *1*, 1096.

(12) Outeiral, C.; Vincent, M. A.; Martín Pendás, Á.; Popelier, P. L. A. Revitalizing the concept of bond order through delocalization measures in real space. *Chem. Sci.* **2018**, *9*, 5517.

(13) Thacker, J. C. R.; Popelier, P. L. A. The ANANKE relative energy gradient (REG) method to automate IQA analysis over configurational change. *Theor. Chem. Acc.* **2017**, *136*, 86.

(14) Hyberts, S. G.; Robson, S. A.; Wagner, G. Exploring signal-to-noise ratio and sensitivity in non-uniformly sampled multi-dimensional NMR spectra. *J. Biomol. NMR* **2013**, *55*, 167.

(15) Hyberts, S. G.; Milbradt, A. G.; Wagner, A. B.; Arthanari, H.; Wagner, G. Application of iterative soft thresholding for fast reconstruction of NMR data non-uniformly sampled with multidimensional Poisson Gap scheduling. *J. Biomol. NMR* **2012**, *52*, 315.

(16) Reed, M. A. C.; Hounslow, A. M.; Sze, K. H.; Barsukov, I. G.; Hosszu, L. L. P.; Clarke, A. R.; Craven, C. J.; Waltho, J. P. Effects of Domain Dissection on the Folding and Stability of the 43 kDa Protein PGK Probed by NMR. *J. Mol. Biol.* **2003**, *330*, 1189.

(17) Williamson, M. P. Using chemical shift perturbation to characterise ligand binding. *Prog. Nucl. Mag. Res. Sp.* **2013**, *73*, 1.

(18) Griffin, J. L.; Bowler, M. W.; Baxter, N. J.; Leigh, K. N.; Dannatt, H. R. W.; Hounslow, A. M.; Blackburn, G. M.; Webster, C. E.; Cliff, M. J.; Waltho, J. P. Near attack conformers dominate β-phosphoglucomutase complexes where geometry and charge distribution reflect those of substrate. *Proc. Natl. Acad. Sci. USA* **2012**, *109*, 6910.

(19) Baxter, N. J.; Bowler, M. W.; Alizadeh, T.; Cliff, M. J.; Hounslow, A. M.; Wu, B.; Berkowitz, D. B.; Williams, N. H.; Blackburn, G. M.; Waltho, J. P. Atomic details of near-transition state conformers for enzyme phosphoryl transfer revealed by MgF_3^- rather than by phosphoranes. *Proc. Natl. Acad. Sci. USA* **2010**, *107*, 4555.

(20) Lakomek, N.-A.; Ying, J.; Bax, A. Measurement of 15N relaxation rates in perdeuterated proteins by TROSY-based methods. *J. Biomol. NMR* **2012**, *53*, 209.

(21) Delaglio, F.; Grzesiek, S.; Vuister, G. W.; Zhu, G.; Pfeifer, J.; Bax, A. NMRPipe: A multidimensional spectral processing system based on UNIX pipes. *J. Biomol. NMR* **1995**, *6*, 277.

(22) Niklasson, M.; Otten, R.; Ahlner, A.; Andresen, C.; Schlagnitweit, J.; Petzold, K.; Lundström, P. Comprehensive analysis of NMR data using advanced line shape fitting. *J. Biomol. NMR* **2017**, *69*, 93.

(23) Lipari, G.; Szabo, A. Model-free approach to the interpretation of nuclear magnetic resonance relaxation in macromolecules. 1. Theory and range of validity. *J. Am. Chem. Soc.* **1982**, *104*, 4546.

(24) Lipari, G.; Szabo, A. Model-free approach to the interpretation of nuclear magnetic resonance relaxation in macromolecules. 2. Analysis of experimental results. *J. Am. Chem. Soc.* **1982**, *104*, 4559.

(25) Halle, B. The physical basis of model-free analysis of NMR relaxation data from proteins and complex fluids. *J. Chem. Phys.* **2009**, *131*, 224507.

(26) Halle, B.; Carlstroem, G. Hydration of ionic surfactant micelles from water oxygen-17 magnetic relaxation. *J. Phys. Chem.* **1981**, *85*, 2142.

(27) Halle, B.; Wennerström, H. Interpretation of magnetic resonance data from water nuclei in heterogeneous systems. *J. Chem. Phys.* **1981**, *75*, 1928.

(28) Halle, B.; Andersson, T.; Forsen, S.; Lindman, B.; Lindman, B. Protein hydration from water oxygen-17 magnetic relaxation. *J. Am. Chem. Soc.* **1981**, *103*, 500.

(29) d'Auvergne, E. J.; Gooley, P. R. The use of model selection in the model-free analysis of protein dynamics. *J. Biomol. NMR* **2003**, *25*, 25.

(30) d'Auvergne, E. J.; Gooley, P. R. Model-free model elimination: A new step in the model-free dynamic analysis of NMR relaxation data. *J. Biomol. NMR* **2006**, *35*, 117.

(31) d'Auvergne, E. J.; Gooley, P. R. Optimisation of NMR dynamic models I. Minimisation algorithms and their performance within the model-free and Brownian rotational diffusion spaces. *J. Biomol. NMR* **2007**, *40*, 107.

(32) d'Auvergne, E. J.; Gooley, P. R. Optimisation of NMR dynamic models II. A new methodology for the dual optimisation of the model-free parameters and the Brownian rotational diffusion tensor. *J. Biomol. NMR* **2008**, *40*, 121.

(33) Bieri, M.; d'Auvergne, E. J.; Gooley, P. R. relaxGUI: a new software for fast and simple NMR relaxation data analysis and calculation of ps-ns and μs motion of proteins. *J. Biomol. NMR* **2011**, *50*, 147.

(34) Clore, G. M.; Szabo, A.; Bax, A.; Kay, L. E.; Driscoll, P. C.; Gronenborn, A. M. Deviations from the simple two-parameter model-free approach to the interpretation of nitrogen-15 nuclear magnetic relaxation of proteins. *J. Am. Chem. Soc.* **1990**, *112*, 4989.

(35) Schwarzinger, S.; Kroon, G. J. A.; Foss, T. R.; Wright, P. E.; Dyson, H. J. Random coil chemical shifts in acidic 8 M urea: Implementation of random coil shift data in NMRView. *J. Biomol. NMR* **2000**, *18*, 43.

(36) Jin, Y.; Bhattasali, D.; Pellegrini, E.; Forget, S. M.; Baxter, N. J.; Cliff, M. J.; Bowler, M. W.; Jakeman, D. L.; Blackburn, G. M.; Waltho, J. P. α-Fluorophosphonates reveal how a phosphomutase conserves transition state conformation over hexose recognition in its two-step reaction. *Proc. Natl. Acad. Sci. USA* **2014**, *111*, 12384.

(37) Blackburn, G. M.; Cherfils, J.; Moss Gerard, P.; Richards Nigel, G. J.; Waltho Jonathan, P.; Williams Nicholas, H.; Wittinghofer, A. How to name atoms in phosphates, polyphosphates, their derivatives and mimics, and transition state analogues for enzyme-catalysed phosphoryl transfer reactions (IUPAC Recommendations 2016). *Pure Appl. Chem.* **2017**, *89*, 653.